Signal, Image and Video Processing manuscript No.
(will be inserted by the editor)

A framework of perceptual features for the characterisation of 3D textured images

Ludovic Paulhac · Pascal Makris · Jean-Yves Ramel · Jean-Marc Gregoire

Received: date / Accepted: date

Abstract This paper presents a multiresolution system for volumetric texture analysis. The originality of this system partially originates from its use of combinations of perceptual texture features that correspond to adjectives commonly used by humans to describe textures. To approximate these features, we use a combination of different families of texture analysis methods rather than a single texture analysis model. This choice is necessary to obtain a good perceptual feature approximation and allows our system to be robust and generic. Moreover, by using our human-understandable features (HUF), it is convenient for a user to manipulate and select the features that are, according to the user, relevant for a given application. Two experiments are presented: the first experiment demonstrates the strong correspondence between our features and a human's description of textures, and the second demonstrates the performance of our proposed method. Finally, the proposed HUF are integrated into an interactive segmentation system and are compared to previously proposed descriptors through analysis of several segmentation results of 3D ultrasound images.

Keywords Volumetric texture · Segmentation · Multiresolution · Human-understandable features · 3D ultrasound images

Ludovic Paulhac
Laboratoire Informatique de l'Université François Rabelais de Tours
64 avenue Jean Portalis - 37200 Tours
Tel.: +332 47 36 14 14
Fax: +332 47 36 14 22
E-mail: ludovic.paulhac@univ-tours.fr

Pascal Makris
Laboratoire Informatique de l'Université François Rabelais de Tours
E-mail: pascal.makris@univ-tours.fr

Jean-Yves Ramel
Laboratoire Informatique de l'Université François Rabelais de Tours
E-mail: jean-yves.ramel@univ-tours.fr

Jean-Marc Gregoire
UMR INSERM U930, CNRS ERL 3106, équipe 5, Université François Rabelais de Tours
E-mail: jean-marc.gregoire@univ-tours.fr

1 Introduction

Texture analysis is widely studied aspect of image analysis and computer vision. Research about this topic continually progresses and concerns a great number of applications in image segmentation and classification. Several methods have been proposed to analyse textures. They are usually classified in four categories [1], statistical methods [2,3], geometrical methods [4], filter based methods [5] and model-based methods [6].
When designing texture analysis techniques, researchers take great care to develop efficient methods but often do not consider the potential user's comfort regarding the term used. Indeed, not everyone can understand the significance of a power spectrum or a bank of filters, for example. Thus, for human-aided applications, it is better to have a set of features that corresponds to those used by humans for describing textures. To obtain general texture measures, some authors [7,8] have proposed understandable 2D texture features. These methods, which are inspired by human texture descriptions, represent a fifth category of texture analysis methods. This last category has been neglected and must be investigated further. New types of images and applications are created often, so methods should be adaptable and interactive.

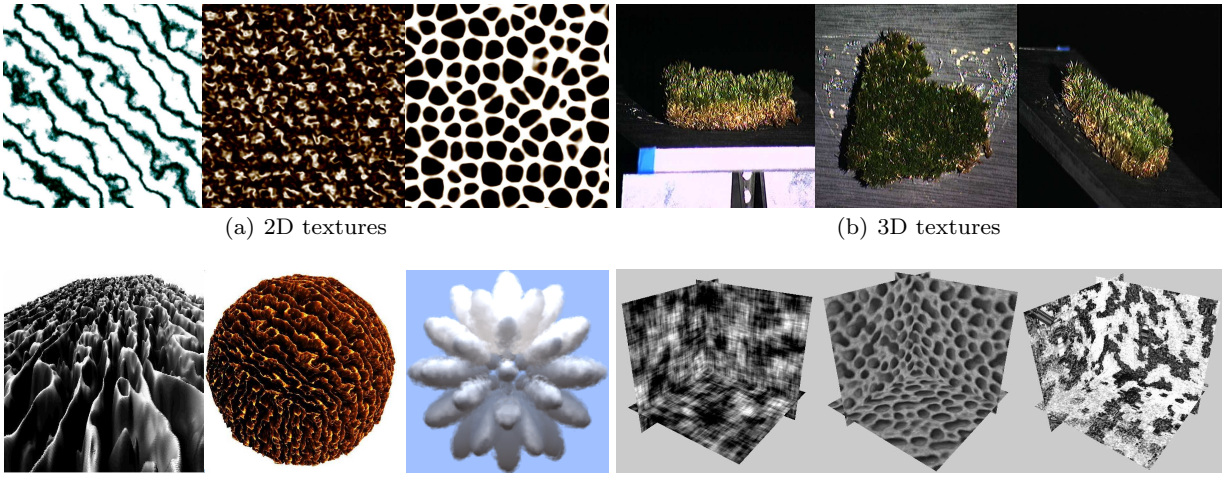

(a) 2D textures (b) 3D textures

(c) Volumic textures (d) Volumetric textures

Fig. 1: Illustration of different representation types of textures: a) represents three different 2D textures, b) shows 3D textures of a same piece of grass viewed from different angles, c) are volumic textures from Neyret homepage [9] and d) represents three different solid/volumetric textures.

Technological advances (including magnetic resonance imaging, digital radiography and ultrasound images) have generated an increasing need for dedicated tools for processing 3D textured images in the medical imaging domain. Consequently, many texture analysis methods for the analysis of volumetric textures have been proposed [10,11,12]. Sometimes referred to as solid textures, volumetric textures can be considered as a set of patterns in a volume (Figure 1 (d)). They represent the external and internal appearance of 3D objects [13]. Solid texture is different from 3D texture or volumetric texturing [14]: 3D texture [15] refers to the observed 2D texture of a 3D object viewed from a particular angle and under different lighting conditions (i.e., photos of the same object under variable conditions), volumetric texturing [16] refers to the rendering of repetitive geometries and reflectance into voxels and is used for modelling complex repetitive geometries such as grass, fur or foliage. 3D textures can also be used to design dynamic textures [17], i.e., sequences of images taken from moving scenes (video).

Our research presents a different approach to the analysis and segmentation of volumetric textures. We propose a set of efficient human understandable features (HUF) to be used in the analysis of different types of volumetric textures. The reason for using perceptual features are numerous and especially concern the interactions with the operator (such as feature selection and contents interpretation). Our initial approach is briefly described in [18]. An improved computation method for geometric features, some additional features and complementary experiments are presented in this work. The most interesting aspect of this work is the proposed multiresolution framework for the computation of perceptual features. This framework allows for the combination and exploitation of different approaches used for texture analysis (i.e., statistical, geometrical and signal processing methods).

Section 2 presents a survey of volumetric texture analysis methods and provides some elements concerning our proposition.

Section 3 describes the framework we propose to compute seven perceptual texture features, each of which is computing using what we considered to be the most appropriate method.

Section 4 presents psychological experiments that demonstrate the correspondence between our texture attributes and human descriptions of textures. Based on these experimental results, additional tests of the correspondence of the proposed texture attributes with human descriptions are proposed.

In section 5, the perceptual features are compared with classical features, known for their efficiency, to validate the performance of our proposed features and to demonstrate their applicability for various problems. Segmentation results for synthetic data and 3D ultrasound images are presented. These results are compared with results obtained using state-of-the-art methods. We conclude with a summary of our research and prospects for future work.

2 Characterization of volumetric textures

2.1 Related work

Much research concerning 2D texture analysis has been conducted, and, some of the proposed methods have also been applied to volumetric textures. In [10], Suzuki *et al* propose extending the higher order local autocorrelation method (HLAC) to three dimensions. 3D data are treated using a 3D HLAC mask which is a solid cube divided into a $3 \times 3 \times 3$ grid. In this method, the texture is analysed locally. However, one problem with the method is that for larger grids (for example $5 \times 5 \times 5$ or $7 \times 7 \times 7$), the number of HLAC mask patterns increases greatly and analysing a texture with a distance greater than 1 becomes difficult.
In [19] Kovalev *et al* propose two approaches to characterise volumetric textures. Their first method uses a 3D orientation histogram that is computed by counting gradient vectors in various orientation bins, whereas their other method is a 3D extension of Chetverikov's co-occurrence matrix method. These two methods are applied to synthetic data that include various levels of noise and to medical images to specifically quantify and monitor the progress of pathologies. The two methods precisely characterise the anisotropy of textures, but in the context of a classification problem, these features should be associated with other texture descriptors.
Additionally, there are many proposed methods that use the 3D grey-level co-occurrence matrix proposed by Haralick [20,21,22,23,24,25]. In [23] Mahmoud-Ghoneim *et al* consider brain tumour classification and compute 2D and 3D Haralick features to compare their respective performances. The 3D Haralick texture features are demonstrated to systematically improve tumour characterisation in comparison with the 2D features, which highlights the importance of the third dimension. Indeed, 3D-based methods provide better information about both the grey-level distribution and the voxels' surroundings. Likewise, in [25] Showalter *et al* use 3D Haralick texture features to predict the micro-architectural properties of bones. For the classification of subcellular location patterns, in [24], Chen and Murphy propose a combination of 3D texture features, 3D Haralick texture features and 3D morphological and edge features. The conclusion of this paper is clear: the combination of different texture analysis methods can improve results.
To analyse volumetric textures, frequency methods have also been used as in [26] where the authors attempt to obtain characteristics of the hippocampus from magnetic resonance images. To do so, they calculate the average energy features using a 2D wavelet transform of each slice of the hippocampus and the energy features produced by a 3D wavelet transform of the hippocampus volume. The authors claim that the 2D wavelet transform provides higher separability compared with 3D wavelet decomposition. In [27], Zhang and Shen present a deformable model to segment 3D ultrasound images. Texture features are computed through the use of two banks of 2D Gabor filters located in two orthogonal planes to reduce the computional time and number of filters required, which can be large for a 3D method. Nevertheless, comparing with a 3D method, using two banks of 2D Gabor filters results in information loss: this is a recurrent problem when two-dimensional methods are extended into 3D. Despite the computational cost required, some authors propose using 3D Gabor filters to segment medical and seismic 3D images [28, 29,12]. In [11], Reyes-Aldasoro and Bhalerao propose characterising volumetric textures by extracting textural measurements from the Fourier domain via subband filtering using an oriented pyramid. This method has been tested on synthetic volumetric images and magnetic resonance images and provides satisfactory results. Their technique demonstrates the usefulness of multiresolution systems and it would be interesting to apply the method to more complex medical images, such as 3D ultrasound images.

The previously presented methods are primarily based on grey-level statistical techniques or filter-based techniques. None of the methods use a system based on human-understandable features. Moreover, the previously presented volumetric texture characterisation methods are primarily used for medical imaging or in domains that require a human-aided applications. Thus, a system that includes human-understandable perceptual features seems particularly relevant because these features should enable significant interactions with an operator (regardless of the operator's technical knowledge concerning image analysis) and efficient feature selection and content interpretation. Similar techniques have been developed [7,8] for 2D texture analysis, but the lack of comparisons with other existing computational methods makes it difficult to evaluate their performance. Moreover, these methods do not consider the multiresolution aspects of textures. These techniques seem to be pertinent, and it would be interesting to attempt to correct the deficiencies of the previously proposed methods. This goal is the purpose of the proposed work which presents a multiresolution system that combines human-understandable features. In the next subsection, we describe the perceptual features used.

Roughness	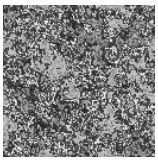	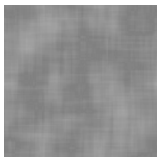	**Contrast**	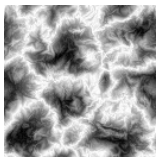	
Granularity	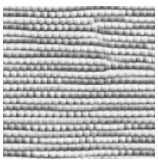	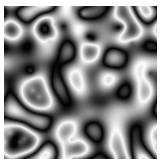	**Regularity**	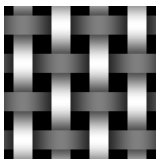	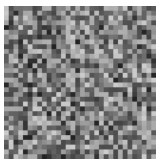
Compactness	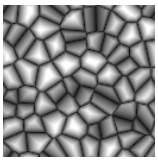		**Volume**		
Directionality	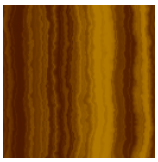	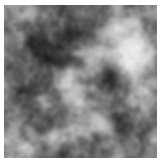			

Table 1: Example of extreme textures for each of the proposed features. Textures on the left obtain a high value for each textural properties and textures on the right a very low value.

2.2 Definitions and considerations regarding the proposed features

We define seven complementary texture features that are inspired by human descriptions of textures. The feature selection was based on the expertise in image analysis acquired from previous research [7,8]. Below, we propose a definition for each of the texture features and we describe their classical approximations. Table 1 presents examples of extreme textures for each of the proposed features. The seven perceptual features we propose are the following:

1) Roughness: *A rough texture is a surface or a volume that has some sharpness (i.e., an uneven surface). Roughness can be described as a set of fast spatial transitions with varying amplitude. The notion of roughness is the opposite of the notion of homogeneity which characterises uniform regions.*
Several methods, including the fractal dimension [30], the Fourier transform [31], and statistical methods [32, 7,8,33,34], have been proposed to analyse and compute roughness.

2) Directionality: *This information describes the prevalence of a privileged direction.*
Many methods to measure texture anisotropy, such as second order statistical methods [3,35,7], the Radon transform [36,37], the autocorrelation function [38], the Hough transform [39], and the wavelet transform [40], have been proposed. The wavelet transforms seems to be the most robust and simplest method to obtain information about direction.

3) Contrast: *This feature is defined as the ratio between the darkest parts and the brightest parts of an image. The contrast is measured by evaluating the grey-level dispersion in an image. In [7], the authors define 4 factors that influence contrast: the range of grey-levels, the ratio of black and white areas, the sharpness of edges, and the period of repetition of patterns.*
This feature is often computed using statistical information about the distribution of grey-level intensity [3, 41,7,8,42].

4) Granularity: *A granular texture is composed of small patterns. This feature is associated with the number of elementary patterns within a texture.*
Several methods allow one to estimate this characteristic. It is possible to use the autocorrelation function [43], fractal methods using the lacunarity feature [44]

and techniques based on connected component extraction [45].

6) Compactness: *This measure describes the shape of patterns and indicates whether the shapes are circular or elongated.*
A geometric study of texture patterns enables an adequate approximation of compactness. Researchers have proposed analysing the connected components inside textures to compute this feature [46,47,48,49].

5) Regularity: *This measure characterises the repetitive nature of a texture.*
A texture's regularity can be measured by studying the repartition and evolution of intensities and by using information about the variation of patterns within the texture. To quantify this feature, methods such as the autocorrelation function [50], the co-occurrence matrix [51] and the binary co-occurrence matrix [52] have been proposed.

7) Volume: *This feature describes the 3D size of the patterns contained in a volumetric texture.*
As for compactness, the volume characterization is often based on the geometric study of patterns [46,47,48, 49].

The first three textural features are related to frequency or statistical analysis of the image, whereas the other four features are computed using information regarding the repetitive patterns that potentially define the texture (these patterns are most often called "textons" [53] and are usually analysed using geometrical methods). By using different families of texture analysis methods, we aim to obtain a good perceptual feature approximation and a robust and generic system that is not limited to only one kind of problem.
These textural properties correspond to adjectives widely used by humans to describe textures. By proposing these texture features, we do not suggest that an optimal description of a given texture is limited to these seven proposed features; additional features could possibly be defined to improve the system. One of our objectives is to address a human-aided approach for classification and segmentation purposes. By using understandable features, it is possible for the user to select the more pertinent features according to the images processed.

3 Definition of computational modes

Texture features that allow one to describe a texture directly depend on the observed resolution. Thus, it is important to use a multiresolution approach to increase the robustness of the framework. The proposed approach uses a multiresolution scheme obtained using a 3D discrete wavelet transform (Figure 2). Separable wavelets are used because they enable one to perform a very fast decomposition by applying a given wavelet function to each of the possible directions. The wavelet function is first applied along the X-axis, then applied along the Y-axis and finally applied along the Z-axis. Non-separable wavelets also exist, but they are less frequently used in image analysis [54]. These wavelets allow for the analysis of several directions, but their computational complexity is greater. **The discrete wavelet transform scheme proposed by Mallat [5] uses different types of filters: a highpass filter allows one to obtain detail coefficients, whereas a lowpass filter yields the approximation coefficients. In 3D, eight images are generated for one level of decomposition: one image for the approximation coefficients and seven images for the detail coefficients. These latter images yield a description of the high frequencies in an image for a given direction.** As illustrated in Figure 2, all of the features are computed for different resolutions to correctly characterise both the macro and micro textures. In our proposed method, the initial image is decomposed using a 3D wavelet transform and the texture features are computed using wavelet sub-bands according to the desired information. The detail coefficients of the wavelet decomposition allow us to compute the roughness and directionality attributes, whereas the other proposed features are computed using the initial image and approximation coefficients of the wavelet decomposition.
Similar to most of texture analysis methods, the features are computed for a given neighbourhood (region). To compute a feature, only the voxels located in a cube of size N^3 centred at the coordinates (x, y, z) are considered. This cube defines the region around the (x, y, z) voxel that is considered (Figure 3).
In the following subsection, the different methods used to compute the proposed volumetric texture features are presented. Different families of texture analysis methods (i.e., statistical, geometrical, and signal processing methods) are exploited to propose a robust system that provides a complete description of textures.

3.1 A geometric characterization of textures

To geometrically characterise textures, the concept of connected components is used. We assume that connected components represent the patch patterns in a texture i.e., the patterns that can be isolated inside a binary texture. Similar to 2D images, the connected

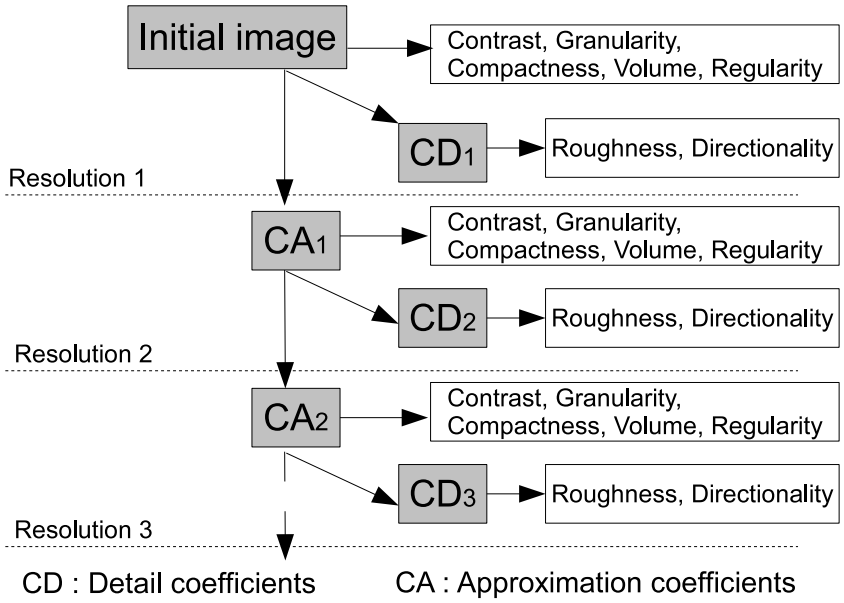

Fig. 2: Multiresolution scheme for texture analysis. Approximation and detail coefficients are computed using a 3D discrete wavelet transform.

components of a 3D image are obtained by assigning the same label to each connected voxel in a black and white image. Figure 4 shows the black and white connected components extracted from a volumetric texture using a global binarisation.
Consider two points A and B that are included in a subset S of an image I. These two points are connected in S if and only if there exists a connecting path in S that links A and B. All of the points inside a connected component satisfy this condition. To extract the connected components, it is necessary to analyse binary images. Several algorithms have been proposed for two-dimensional images; the main ones are presented by Chassery and Montanvert in [55]. From these methods, we choose to adapt to 3D images an algorithm that only requires two scans to process an image. This two pass algorithm [56] operates in three distinct phases: a scanning phase to assign provisional labels, an analysis phase to determine the label equivalence information and a labelling phase to assign the final labels. For this algorithm, the complexity depends on the size of the image, whereas for a sequential algorithm, the number of iterations depends on the complexity of the objects.

To obtain connected components that are as representative of the texture as possible, the grey-level image is decomposed into a sequence of successive binary images. A similar approach has been proposed by Shoshany in [45] but it was proposed only for texture classification. His method constructs a binary sequence using all of the possible grey-level values (256 values); however, for segmentation applications, the resulting number of binary images is intractable. Moreover, Shoshany uses three features that are based on the connected components obtained for each binary image (256×3 features). Our purpose is different because we intend to extract the geometrical features of a 3D texture from the connected components. Thus, it is more interesting and efficient to detect the primary grey-level classes of an image to identify a set of optimised binarisation. A clustering algorithm is used to determine the primary grey-level classes within 3D images. **The proposed method uses the k-means algorithm with a high value for k to obtain the voxel clusters that are the most representative in the processed image. Figure 5 shows grey-level histograms of the clustered image obtained after replacing the voxel values in each cluster by the centroid values. Only maxima upper than the average pixel repartition are considered and thresholds t_i are selected between all the pairs of these maxima. By this way, non-representative clusters are ignored and the obtained threshold values (for different values of k) are very stable as illustrated Figure 5(a) and Figure 5(b)**. The threshold selection is important because it significantly increases the robustness of the proposed features. This component of our segmentation framework, which geometrically characterises volumetric textures, another contribution of this work. Using a classical global or

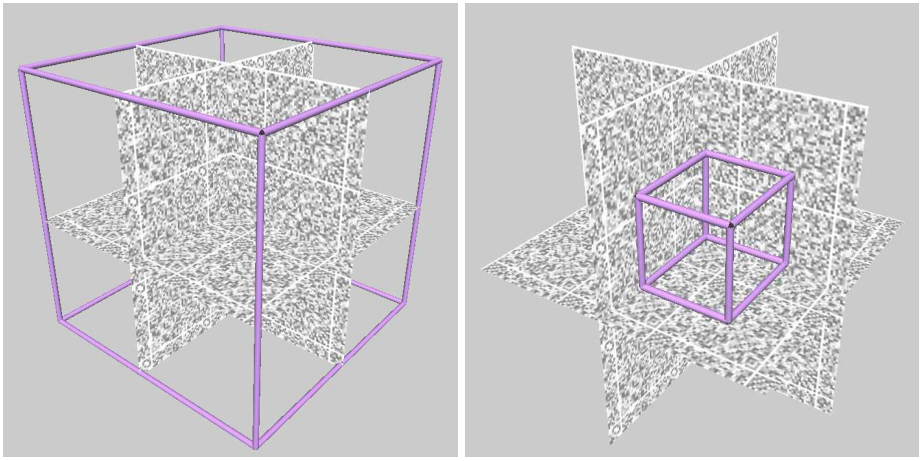

(a) Texture features are computed using the entire image

(b) Texture features are computed using a part of the image

Fig. 3: Examples of two regions in a same volumetric texture.

local binarisation algorithm or the Shoshany method does not allow one to compute stable geometrical features because a single binary image does not provide enough information about the structure of an image. When considering the 256 possible thresholds, most information is lost, and it is very difficult to compute geometrical features from such a large set of binary images.

A grey-level texture is then decomposed into a succession of binary images using progressive thresholding. The connected components and the associated texture features (granularity, volume, compactness and regularity) are computed for each binary image produced. Formally, we consider a grey-level image I_β at resolution β and the set of corresponding 3D binary images B_β. The Q_β binary images $B_{i,\beta}$, where $i = \{1..Q_\beta\}$, are composed of a set of connected components $CC_{i,\beta}$ where $P_{i,\beta}$ is the number of connected components in $B_{i,\beta}$. A set of 4 structural features $EF_{i,\beta} = \{f_{gran_{i,\beta}}, f_{comp_{i,\beta}}, f_{reg_{i,\beta}}, f_{vol_{i,\beta}}\}$ which correspond to the granularity, the compactness, the regularity and the volume, is then associated with each $CC_{i,\beta}$.

Some of the binary images generated contain a great number of connected components and therefore provide important structural information. Conversely, a binary image with a unique connected component provides very little structural information. To emphasise the most interesting binary images, texture features computed using the sequence of binary images are weighted using the number of connected components considered. The values of the geometric features associated with the voxel (x, y, z) for the resolution β are computed as follows:

$$f_{gran_\beta}(x,y,z) = \sum_{i=1}^{Q_\beta} \frac{P_{i,\beta}}{\max_i(P_{i,\beta})} f_{gran_{i,\beta}}(x,y,z) \quad (1)$$

$$f_{comp_\beta}(x,y,z) = \sum_{i=1}^{Q_\beta} \frac{P_{i,\beta}}{\max_i(P_{i,\beta})} f_{comp_{i,\beta}}(x,y,z) \quad (2)$$

$$f_{reg_\beta}(x,y,z) = \sum_{i=1}^{Q_\beta} \frac{P_{i,\beta}}{\max_i(P_{i,\beta})} f_{reg_{i,\beta}}(x,y,z) \quad (3)$$

$$f_{vol_\beta}(x,y,z) = \sum_{i=1}^{Q_\beta} \frac{P_{i,\beta}}{\max_i(P_{i,\beta})} f_{vol_{i,\beta}}(x,y,z) \quad (4)$$

$P_{i,\beta}$ represents the number of connected components in the binary image $B_{i,\beta}$.

$f_{gran_{i,\beta}}$ is computed for each binary image i and corresponds to the number of connected components per unit volume:

$$f_{gran_{i,\beta}}(x,y,z) = \frac{P_{i,\beta}}{N^3} \quad (5)$$

Only the connected components located in a cube of size N^3 centered at the coordinates (x, y, z) (regionality around one voxel) are considered.

The volume corresponds to the size occupied by the

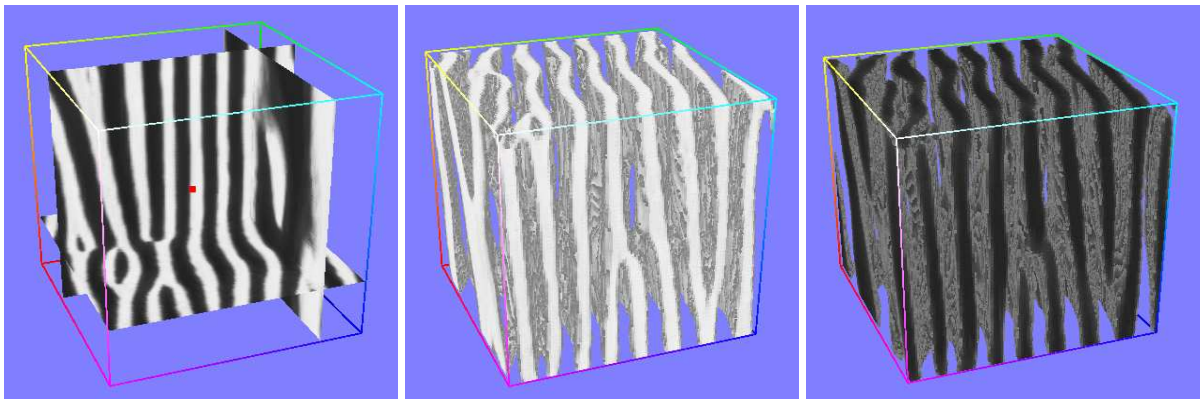

(a) (b) (c)

Fig. 4: a) A volumetric texture, b) White connected components after a global binarisation, c) Black connected components after a global binarisation. Connected components are used in our framework to compute granularity, compactness, volume and regularity features (see sub-section 3.1 for more details).

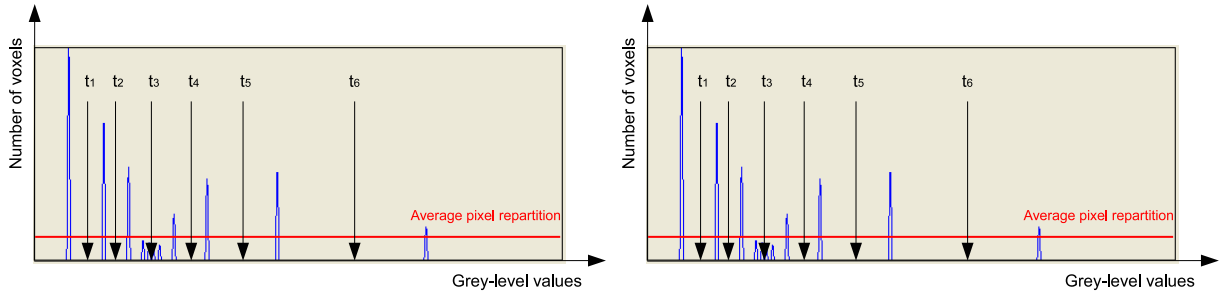

(a) (b)

Fig. 5: Histograms of a clustered image obtained using a k-means on 3D image voxels and after replacing the voxel values in each cluster by the centroid values. For high values of k, one can observe the stability of the obtained histograms (in (a) $k = 20$ and in (b) $k = 40$). An histogram allows to select the thresholds t_i and then to construct a sequence of successive binary images (see the sub-section 3.1 for more details).

patterns that constitute the volumetric textures. It is computed as follows [46,47,48,49]:

$$f_{vol_{i,\beta}}(x,y,z) = \frac{1}{P_{i,\beta}} \sum_{\alpha=1}^{P_{i,\beta}} V_{\alpha,i,\beta} \tag{6}$$

where $V_{\alpha,i,\beta}$ corresponds to the volume of a connected component $CC_{i,\beta}$.

The compactness of connected components provides information about the shape of the patterns that constitute the texture. For a pattern, this feature can be computed using the ratio between its surface and its volume [46,47,48,49]. A texture with an elongated shape has low compactness. To obtain the compactness feature of a texture, we compute the average compactness of the patterns inside the texture. In a 3D domain, the compactness can be computed as follows:

$$f_{comp_{i,\beta}}(x,y,z) = \frac{1}{P_{i,\beta}} \sum_{\alpha=1}^{P_{i,\beta}} \frac{S_{\alpha,i,\beta}^{\frac{3}{2}}}{V_{\alpha,i,\beta}} \tag{7}$$

where $S_{\alpha,i,\beta}$ is the surface of a connected component $CC_{i,\beta}$.

To obtain an approximation of the regularity of the texture, the variance of the compactness is used. Because the compactness is invariant under any transformation [57], the variations in shape are the only elements that affect the variance feature. We wish to study the pattern shape stability. For a given texture, if the variance is low, the patterns are very similar and the texture is very regular. The regularity is given by the following

formula:

$$f_{reg_{i,\beta}}(x,y,z) = \underset{\alpha}{\text{variance}}\left(\frac{S^{\frac{3}{2}}_{\alpha,i,\beta}}{V_{\alpha,i,\beta}}\right) \tag{8}$$

3.2 Statistical and frequency based methods for measuring roughness and contrast

Filter-based methods are known to be efficient and to provide local and global information about the textures studied. In [5,54], Mallat suggested the use of pyramid-structured wavelet transform for texture analysis. This decomposition scheme uses different types of filters: a highpass filter allows one to obtain detail coefficients, whereas a low-pass filter yields the approximation coefficients. In 3D, eight images are generated for one level of decomposition: one image for the approximation coefficients and seven images for the detail coefficients. These latter images yield a description of the high frequencies in an image for a given direction.

The decomposition process presented in Figure 2 provides a set of detail sub-bands that are used to compute the roughness and directionality features. In an image, roughness can be described as a set of fast spatial transitions with different amplitudes. The image sharpness in the spatial domain correspond to the presence of high frequencies. Knowing the detail coefficients of a wavelet transform enables the identification of high frequencies. The roughness feature is computed as follows:

$$f_{rgh_\beta}(x,y,z) = \sum_{l=1}^{M}\Big(\sum_{i,j,k=1}^{N} |w_{l,\beta}(i,j,k)|\Big)/M \tag{9}$$

where $w_{l,\beta}(i,j,k)$ corresponds to the set of detail coefficients for the voxel (x,y,z) (cube of size N^3) for the sub-band l. M is the number of detail coefficient sub-bands for a given resolution.

Likewise, detail sub-bands can provide information about directionality. In 3D, the seven detail sub-bands describe seven different directions. To incorporate the directionality feature in our framework, the following formula is used:

$$f_{dir_\beta}(x,y,z) = \max_{l}\Big(\sum_{i,j,k=1}^{N} |w_{l,\beta}(i,j,k)|\Big) - f_{rgh_\beta}(x,y,z) \tag{10}$$

In [2,3], Haralick proposes an estimation of contrast that uses second order statistics. The moment of inertia is computed from the main diagonal of the co-occurrence matrix. However, the construction of a co-occurrence matrix for the sole estimation of the contrast can be computationally expensive. In [7], Tamura identifies four factors that influence the contrast difference between two textures. To approximate the contrast, they propose a measure that incorporates the two first factors: the range of grey-levels and the ratio of black and white areas.
To obtain a measure of polarisation, they use the kurtosis α_4. This enables a measurement of the disposition of probability mass around their center.

$$\alpha_{4,\beta} = \frac{\mu_{4,\beta}}{\sigma^4_\beta} \tag{11}$$

where μ_4 is the fourth central moment and σ^2 is the variance of grey-levels for the resolution β. To take into account the dynamic range of grey-levels, they combine the kurtosis with the standard deviation of grey-levels as follows:

$$f_{cont_\beta}(x,y,z) = \frac{\sigma_\beta}{\alpha^n_{4,\beta}} \tag{12}$$

where n is a positive value. In their paper, Tamura et al. compare psychological experiments and their operators and conclude that the value $n = 1/4$ yields the best approximation. As for the other features, the values of σ_β and $\alpha^n_{4,\beta}$ are computed in a cube of size N^3 around the considered voxel (x,y,z).

Finally, we obtain seven perceptual features that correspond to adjectives commonly used to describe textures (f_{cont}, f_{gran}, f_{rgh}, f_{comp}, f_{vol}, f_{reg}, f_{dir}). In the next section, psychological experiments are presented to demonstrate the strong correspondence between human characterization of textures and the HUF (human-understandable feature) description provided by our framework.

4 Psychological experiments

The proposed visual features are inspired by manner in which humans describe textures. It is thus necessary to study the correspondence between values assigned automatically to these features and the estimation of these textures through human vision. For verification, psychological experiments were performed. A questionnaire, that contained 12 volumetric textures of size 128^3 voxels with 256 grey-levels was created and distributed to a group of 26 persons. The questionnaire contained textures that were constructed using methods presented in [58,59], except for textures (j) and (l) which corresponded to ultrasound images (Figure 6). To obtain an adequate resolution, these questionnaires were printed

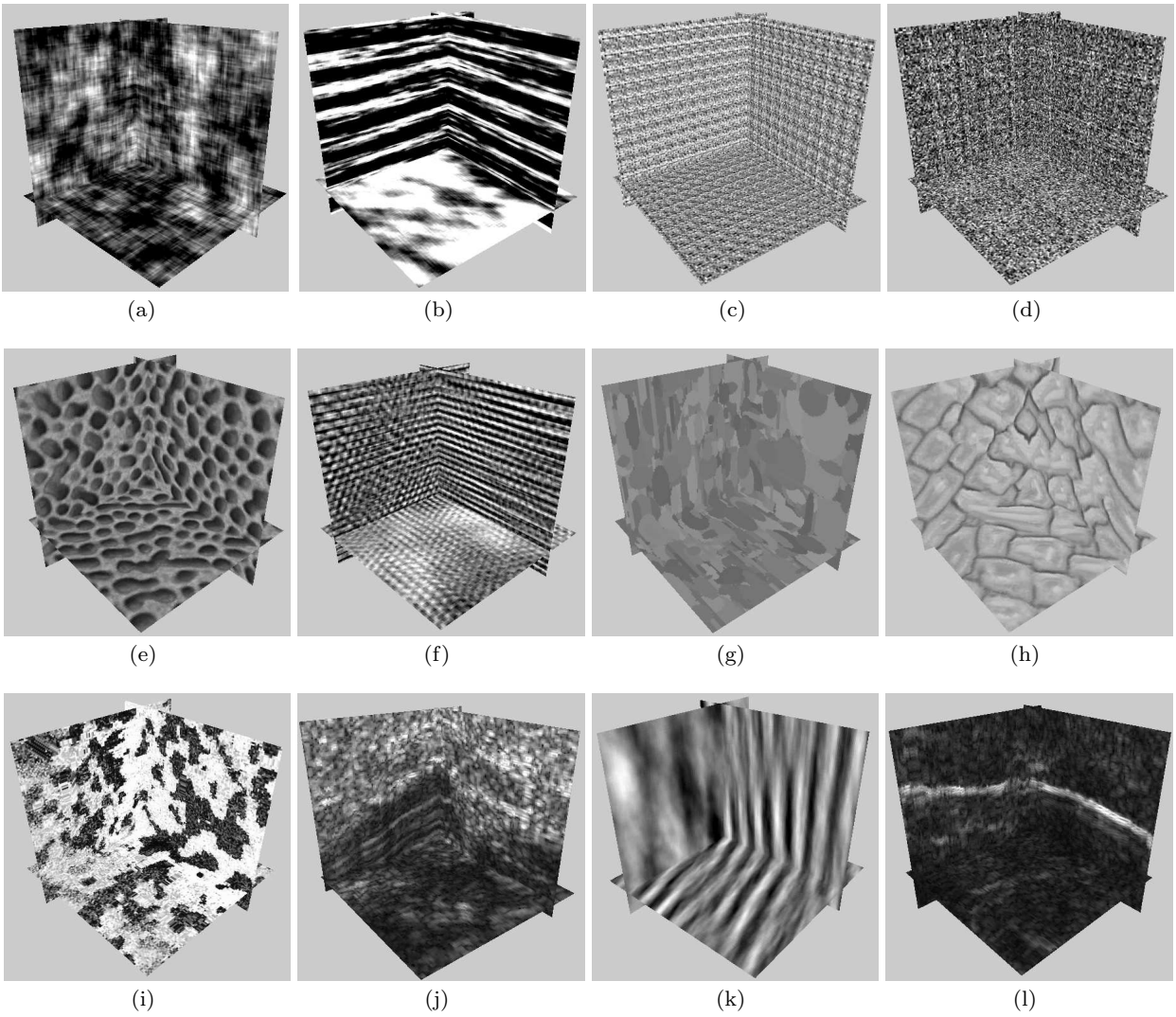

Fig. 6: Set of Solid textures used for psychological experiments. These textures of size 128^3 voxels with 256 gray-levels have been printed on a questionnaire and distributed to a group of 26 persons. For each feature, the images were ranked by the human subjects for a comparison with our computational ranking.

using a high quality colour printer.
For each feature, the images were ranked by the human subjects in descending order, e.g., from the roughest to the smoothest, from the most regular to the most irregular and so forth. Before the questionnaire was administered, the features defined above and the purpose of these experiments were explained to the human subjects. A ranking of the twelve textures was defined for each feature based on the answers to the questionnaire. For a given feature, a score was assigned to a texture according to its rank. For example, the most compact texture was assigned the value +12 (for the compactness feature), the second most compact texture +11 and finally the least compact texture received a score of +1. All features were scored in the same manner. The addition of the questionnaires' scores for each texture resulted in a final ranking for a given feature. A similar feature ranking was also generated using the proposed framework. Texture attributes were computed for a region corresponding to the entire image, and each 3D image was then described using the seven features. Texture features were generated for the first resolution (i.e., the highest resolution) and the second resolution ($\beta = 1$ and $\beta = 2$) as depicted in Figure 2 to analyse the possible variation in the correlation with resolution. Tests of the correlation were then generated using the seven texture features for the first resolution (Table 2) and the seven texture features for the second resolution (Table 3).

4.1 Comparison between human and feature rankings

To compare the computational ranking with the human ranking, the degree of correspondence between the rankings was computed. For this purpose, Spearman's rank correlation coefficient was used. The coefficient is given by:

$$r_s = 1 - \frac{6}{n^3 - n} \sum_{i=1}^{n} d_i^2 \tag{13}$$

where n is the number of individuals and d_i is the difference between the ranks assigned to the ith object in the two measurements. This coefficient has a value between -1 and 1: a value of 1 indicating a complete correlation between the two types of ranking whereas value -1 indicates complete disagreement.

Tables 2 and 3 present the rank correlation between the feature ranking and the representative human ranking for each textural property. The results (Table 2) indicate an important correlation between the human and feature rankings (for the features computed at the first resolution). The best correspondence is obtained for the compactness feature, which has a Spearman's coefficient value of 0.9; this result indicates a strong link between the two rankings with a confidence rate of 100 percent. Unsurprisingly, the lowest correspondences was obtained for the volume, which is most likely the feature that is the most difficult for a human to evaluate. Nevertheless, Spearman's coefficient indicates that there is a link between the human ranking and the feature ranking with a confidence rate between 95 and 98 percent.
In Table 3, the rank correlations coefficients between the human and feature rankings are presented for the features computed only at the second resolution. The correlations between the two rankings are less than for the higher resolution, but they are sufficiently strong. The texture size in the images printed in the questionnaire corresponds to the texture size of the first resolution analysed using our framework. When observing the volumetric texture of the images on the questionnaire, the subjects had a perception of textures that was very similar to the highest resolution used in our framework. Indeed, the subjects observed the volumetric textures at the highest resolution possible. The correspondence of the resolution of the printed images with the highest resolution used in our framework is the reason the correlation between the human and feature rankings is the highest for the first resolution. If we had asked the subjects to analyse the questionnaire from a greater physical distance, the results would most likely change; the correlation between the human ranking and the feature ranking for the second resolution would likely increase. Table 4 illustrates the correlations between each feature computed using the feature ranking. Table 5 shows the correlations computed using the human ranking. There are correlations between roughness, compactness and granularity in both the feature and human rankings. This is also the case in Tables 2 and 3. A granular texture, i.e., texture with a greater number of patterns, can, in some cases, have some irregularities and can thus appear rough. However, the correlation is not sufficiently significant to eliminate one of these texture attributes. Moreover, it is possible to find a set of volumetric textures with a high compactness value and a low roughness value (and vice versa). The directionality has a weak correlation with the other features; it is most strongly correlated with the contrast (which was expected because: if a texture is anisotropic then a strong contrast reinforces the directional module).
By considering these results, and knowing that the user will have to select a subset of the proposed features, we have decided to keep all these features in our framework even if there is some correlation between some of them.

	f_{gran}	f_{comp}	f_{vol}	f_{reg}	f_{rgh}	f_{cont}	f_{dir}
f_{gran}	0.83	0.63	−0.48	0.28	0.66	0.01	−0.01
f_{comp}	0.66	0.90	−0.39	0.59	0.63	−0.30	−0.15
f_{vol}	−0.57	−0.49	0.61	−0.48	−0.56	0.43	−0.22
f_{reg}	0.41	0.44	−0.37	0.82	0.55	0.23	0.47
f_{rgh}	0.70	0.57	−0.50	0.45	0.75	0.07	0.25
f_{cont}	−0.09	−0.38	0.48	−0.29	0.24	0.65	0.35
f_{dir}	−0.36	−0.28	0.29	−0.07	−0.02	0.29	0.70

Table 2: Rank correlation coefficients between human and feature rankings (resolution 1).

	f_{gran}	f_{comp}	f_{vol}	f_{reg}	f_{rgh}	f_{cont}	f_{dir}
f_{gran}	0.73	0.48	−0.19	0.16	0.49	−0.06	0.16
f_{comp}	0.51	0.66	−0.32	0.18	0.49	−0.21	0.11
f_{vol}	−0.37	−0.1	0.42	−0.27	−0.4	0.38	−0.3
f_{reg}	0.29	0.3	−0.39	0.61	0.45	−0.24	0.12
f_{rgh}	0.43	0.47	−0.5	0.38	0.71	0.12	0.18
f_{cont}	0.02	−0.36	0.42	−0.2	0.33	0.45	0.3
f_{dir}	0.06	−0.3	0.18	−0.15	0.21	0.32	0.60

Table 3: Rank correlation coefficients between human and feature rankings (resolution 2).

5 Quantitative evaluation of the proposed combination of features

The previous section demonstrates the perceptual aspects of the proposed features that result in a robust qualitative description of volumetric textures. In this section, we propose a quantitative evaluation of the ro-

	f_{rgh}	f_{comp}	f_{vol}	f_{reg}	f_{cont}	f_{dir}
f_{gran}	0.67	0.63	−0.53	0.47	−0.01	−0.02
f_{dir}	0.29	0.18	−0.13	0.29	0.34	–
f_{cont}	−0.17	−0.25	0.47	−0.23	–	–
f_{reg}	0.57	0.59	−0.52	–	–	–
f_{vol}	−0.42	−0.45	–	–	–	–
f_{comp}	0.59	–	–	–	–	–

Table 4: Rank correlation coefficients between the different feature rankings (resolution 1).

	f_{rgh}	f_{comp}	f_{vol}	f_{reg}	f_{cont}	f_{dir}
f_{gran}	0.73	0.67	−0.39	0.52	0.13	−0.35
f_{dir}	−0.17	−0.24	−0.32	0.08	0.42	–
f_{cont}	0.28	−0.24	0.12	−0.03	–	–
f_{reg}	0.52	0.50	−0.25	–	–	–
f_{vol}	−0.55	−0.48	–	–	–	–
f_{comp}	0.60	–	–	–	–	–

Table 5: Rank correlation coefficients between the different human rankings.

bustness of the proposed framework using segmentation experimentations. Our framework (the HUF method) is compared with previously proposed texture analysis methods, the 3D grey-level co-occurrence matrix of Haralick (3DGLCM), a 3D extension of the local binary pattern method (3DLBP) [60] and the 3D discrete wavelet transform (3D DWT) [5,26].
These tests of segmentation were performed using a set of synthetic volumetric textures. We present quantitative evaluations obtained using recognised evaluation criteria. To perform these experiments, because of the lack of an existing database, it was necessary to construct a volumetric texture database. This contribution is described in the following subsection.

5.1 A solid texture database for segmentation and classification experiments

Among the existing databases, the most well-known are specifically two-dimensional: the Brodatz database [61], the Randen database [62] and the Meastex database [63] have often been used because of their richness. Databases of 3D textures and volumic textures are also available. Among the 3D databases, PMTex [64], CURet [65] and OUTex [66] are considered references. Several volumic textures are available on the Neyret's homepage [9]. Johannes Kopf also proposes some examples of solid textures in [67] but currently, there are too few images to perform significant classification or segmentation experiments.
Three different types of textures have been identified in previous research [68]: deterministic textures, which are characterised by the repetition of similar patterns; stochastic textures, which are identified by their irregularity; and observable textures, which are a mix of textures from the two previous categories. To construct a complete database, synthetic images that are representative of these three classes were created using four simple methods. To limit memory and processing time required, the volumetric textures have a size of 64^3. Considering the classification tests performed in previous research, this size seems to be sufficient for classification experiments. Currently, 95 classes of solid textures are available in our database and each class contains 50 examples that include transformations. To enable segmentation experiments, we also provide 3D images of size 128^3 that contain several classes of volumetric textures. Finally, it is important to note that the purpose of this database is not to provide volumetric textures that are as realistic as possible but to provide solid textures of many classes to allow an evaluation of the properties and performance of volumetric texture analysis methods. This database is freely available at [69] and additional information can be found in [59].

5.2 Evaluation for segmentation purpose

Our HUF method was compared with three methods of volumetric texture analysis: the 3D grey-level co-occurence matrix of Haralick [2,3] (3D GLCM), the 3D LBP method [60] and the 3D Discrete Wavelet Transform (3D DWT) [5,26]. The segmentation results were produced using fifteen different 3D images (Figure 7) generated using volumetric textures from our database. Five of the 3D images contained two classes of textures, five of the 3D images contained three classes of textures and the remaining five contained four classes of textures. The 3D GLCM method requires two parameters to be adjusted: the distance between two voxels, d, and a parameter of grey-level quantification, q. Using the co-occurrence matrix, the following texture features were computed: the angular second moment, the variance, the contrast, the correlation, the entropy, the homogeneity, the sum average, the sum entropy, and the uniformity. As in [70], $LBP^{riu2}_{P',R}$ operator was tested using three different spatial resolutions and three angular resolutions. For a given radius, if the number of vertices is too small, then the probability of obtaining a uniform pattern decreases. The three operators $LBP^{riu2}_{26,1}$, $LBP^{riu2}_{98,2}$ and $LBP^{riu2}_{218,3}$ were computed where $V \in \{2,3\}$. The LBP methods allow one to characterise a texture using the LBP histogram, which contains the statistical repartition of local binary patterns in a texture. For the DWT and HUF methods, the wavelets of Haar and Daubechies [71,72] were used with different resolutions. For the DWT method, the norm-1

energy [73] was computed for each sub-band of the decomposition (detail coefficients and approximation coefficients). For the HUF method, the set of texture features presented in section 3 was used: granularity, volume, compactness, regularity, contrast, roughness, and directionality. Finally, different values of region size N (which defines the neighbourhood around each voxel) were tested.

5.2.1 Exploiting the multiresolution schema for texture segmentation

As explained in section 3, the proposed approach enables one to obtain a set of seven features for each resolution. A 3D discrete wavelet transform is used to compute the HUF using the detail and approximation coefficients of the generated sub-bands. For segmentation, the features are computed for each voxel of the processed image. To maintain the same number of texture attributes, for any resolution, an upsampling step is necessary (Figure 8). A voxel is then described by a vector that contains $7n$ texture features, where n is the number of resolutions and 7 is the number of proposed perceptual features: the granularity (f_{gran}), the shape information of patterns (f_{vol} and f_{comp}), the regularity of these patterns (f_{reg}), the contrast (f_{con}), the roughness (f_{rgh}) and the directionality (f_{dir}). To produce the segmentation, a clustering of the voxels was performed. the k-means algorithm [74] was used to classify the voxels in subsets according to their texture characteristics. The processing time for volumetric textures can sometimes be very long, and the primary advantages of the k-means method are its speed and its low memory requirements. In terms of performance, the k-means algorithm does not guarantee that a global optimum will be found, but it yields an efficient clustering of voxels in a low execution time. Because this method requires a number of expected classes as input, we use a large number of classes to obtain an initial segmentation as a first solution to the problem. Then, a merging of classes can be achieved by using an ascendant hierarchical classification and the two most similar regions are merged at each step. The distances between the regions are computed using the features that correspond to the centroid of each class. Using a simple interface, the user of the software can decide when to stop the merging process to obtain the desired segmentation.

5.2.2 Presentation of segmentation results

In the proposed evaluation, the combination between the k-means algorithm and the ascendant hierarchical classification is also used for the GLCM, DWT and LBP methods. For each segmentation generated, the user chooses the number of necessary merges to obtain the segmentation that is most similar to the ground truth. To evaluate the segmentation, the generic discrepancy measure [75] is used as the performance measure. This measure computes a distance between partitions that was defined by Gusfield [76] as follows:

Definition 1 Given two partitions P and Q of S, the partition distance is the minimum number of elements that must be deleted from S, such that the two induced partitions (P and Q restricted to the remaining elements) are identical.

The generic discrepancy measure corresponds to the normalised partition distance. If two partitions P and Q are considered, then the generic discrepancy measure d_{gdm} is defined as follows:

$$d_{gdm} = d_{sym}(P, Q)/(N - 1) \tag{14}$$

where N is the number of voxels and d_{sym} is the partition distance that corresponds to the number of misclassified voxels. Moreover, d_{sym} has the following properties [75]:

- $d_{sym}(P, Q) >= 0$,
- $d_{sym}(P, Q) = 0$ if and only if $P = P'$,
- $d_{sym}(P, Q) = d_{sym}(Q, P)$,
- $d_{sym}(P$,null partition$) = N -$ (the maximal cluster size in P),
- $d_{sym}(P$, infinite partition$) = N -$ (the number of clusters in P),
- d_{sym}(null partition, infinite partition$) = N - 1$.

A "null partition" is a partition that contains only one cluster and the "infinite partition" is the partition that contains N clusters. If d_{gdm} is equal to 0, the segmentation is ideal. An inverse segmentation generates the value 1 which is only possible if P corresponds to the null partition and Q corresponds to the infinite partition or vice versa.

Segmentation results are presented in three tables: Table 6 shows the evaluation results computed using 3D images with two classes of volumetric textures, Table 7 presents the results computed using segmentation of 3D images with three classes, and Table 8 illustrates the quality of the segmentation obtained using 3D images with four classes. Table 9 shows the mean and the standard deviation of the normalised partition distance obtained for the segmentation results in Tables 6, 7 and 8 where different parameters of the LBP, DWT, HUF and GLCM methods are tested. To make the results more readable, the results of the generic discrepancy measure have been multiplied by 100.

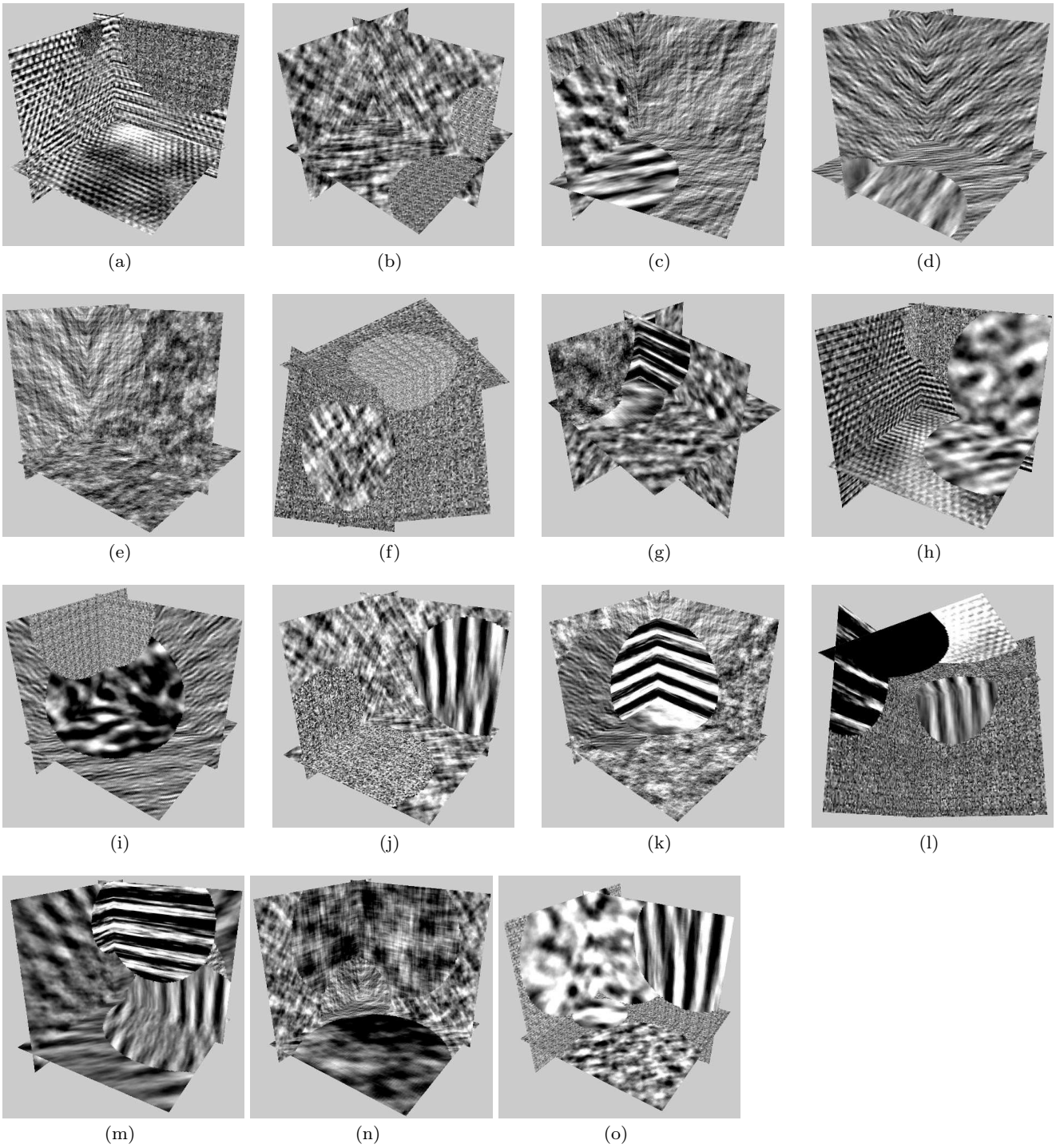

Fig. 7: Solid texture images used in the segmentation experiments section 5: [a-e] 2 classes of textures, [f-j] 3 classes of textures, [k-o] 4 classes of textures.

For all of the segmentations presented in the tables 6, 7 and 8, the segmentation results obtained with the 3D GLCM method are lower than those obtained by the 3D LBP, 3D DWT and HUF methods. The 3D LBP, 3D DWT and HUF methods obtained the best segmentation results and the HUF and 3D DWT methods performed best if all of the processed 3D images are considered. For textures that are relatively easy to segment i.e., those with two classes, the 3D LBP method obtained good results, which are similar to the results

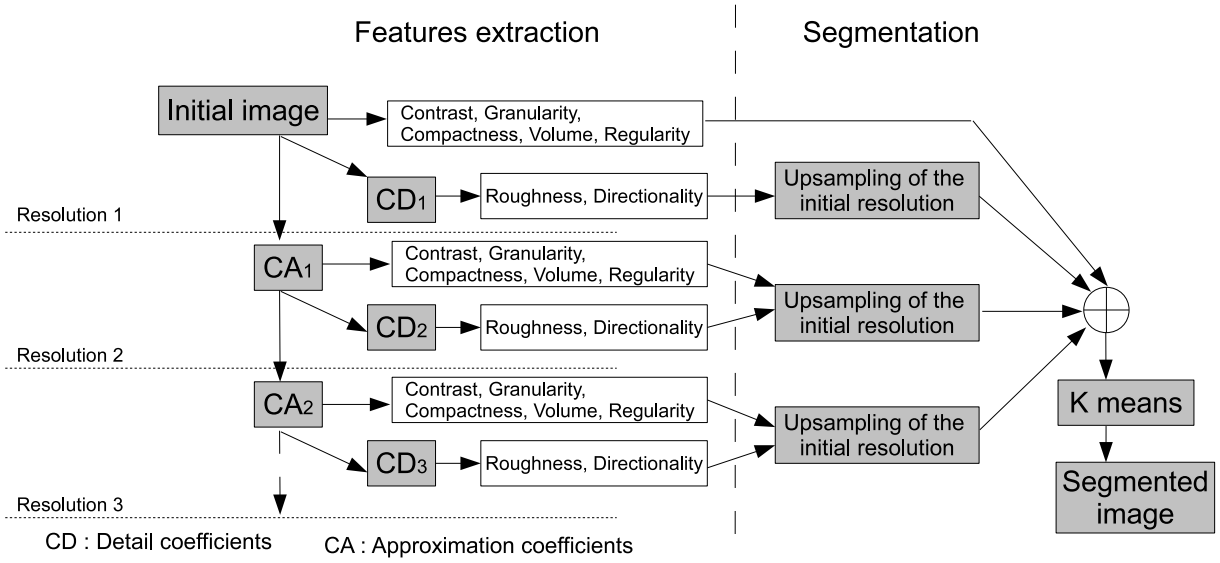

Fig. 8: Using the HUF framework for segmentation: on the left we can observe our multiresolution scheme to compute the HUF features, on the right we have a step of feature upsampling and a clustering algorithm to obtain a segmentation.

Methods	(a)	(b)	(c)	(d)	(e)
$LBP^{riu2}_{26,1}$, N=5	0.88	0.60	2.96	2.36	30.82
$LBP^{riu2}_{26,1}$, N=7	0.74	0.50	**1.18**	0.95	21.49
$LBP^{riu2}_{26,1}$, N=9	2.23	0.72	1.43	0.97	20.25
$LBP^{riu2}_{98,2}$, N=5	1.23	0.78	3.74	3.32	31.88
$LBP^{riu2}_{98,2}$, N=7	1.33	0.51	2.48	2.35	20.88
$LBP^{riu2}_{98,2}$, N=9	6.87	**0.46**	2.06	0.76	19.68
DWT, db2, $\beta = 1$, N=5	2.49	0.54	1.91	2.53	15.35
DWT, db2, $\beta = 1$, N=7	2.20	0.52	1.94	**0.50**	18.62
DWT, db2, $\beta = 1$, N=9	2.24	0.50	1.98	0.52	31.74
DWT, db2, $\beta = 2$, N={5,7}	3.25	1.85	2.54	2.42	13.06
DWT, haar, $\beta = 1$, N=5	2.55	0.64	2.22	2.60	16.93
DWT, haar, $\beta = 1$, N=7	2.33	0.57	2.32	0.61	20.26
DWT, haar, $\beta = 1$, N=9	2.40	0.51	2.34	0.55	32.30
DWT, haar, $\beta = 2$, N={5,7}	3.35	2.25	4.01	2.45	14.81
HUF, db2, $\beta = 1$, N=5	0.91	1.73	8.31	2.07	27.35
HUF, db2, $\beta = 1$, N=7	**0.71**	0.60	8.42	2.00	16.70
HUF, db2, $\beta = 1$, N=9	1.12	0.50	2.09	1.04	16.18
HUF, db2, $\beta = 2$, N={5,7},	1.30	0.87	1.87	0.72	**12.45**
HUF, haar, $\beta = 1$, N=5	2.52	1.26	16.78	2.34	27.82
HUF, haar, $\beta = 1$, N=7	2.00	1.30	8.26	2.76	17.31
HUF, haar, $\beta = 1$, N=9	5.96	2.57	2.60	1.51	30.32
HUF, haar, $\beta = 2$, N={5,7}	4.25	2.39	9.17	1.98	14.65
GLCM, $q = 8$, $d = 1$, N=5	0.87	9.75	17.50	3.40	36.66
GLCM, $q = 8$, $d = 1$, N=7	1.14	3.95	3.83	2.60	31.28
GLCM, $q = 8$, $d = 1$, N=9	1.00	0.87	9.29	2.99	32.23
GLCM, $q = 8$, $d = 2$, N=5	1.24	54.16	21.30	12.33	29.83
GLCM, $q = 8$, $d = 2$, N=7	4.10	33.91	13.82	43.08	32.46
GLCM, $q = 8$, $d = 2$, N=9	18.46	42.33	22.13	12.34	33.63

Table 6: Evaluation of solid texture segmentations using the normalized partition distance (texture with 2 classes). For each texture, the bold values show the best evaluation values (the best segmentation).

obtained using the HUF and 3D DWT methods. However, for complex volumetric textures (those that contain more classes), such as textures (m) and (n), the 3D LBP method was outperformed by the HUF and 3D DWT methods. Indeed, the HUF and 3D DWT methods yielded accurate results for all of the processed textures, and for the complex textures, the segmentation results were very satisfactory in comparison with

Methods	(f)	(g)	(h)	(i)	(j)
$LBP^{riu2}_{26,1}$, N=5	9.76	6.19	6.71	29.69	11.18
$LBP^{riu2}_{26,1}$, N=7	9.72	5.51	3.01	15.08	17.31
$LBP^{riu2}_{26,1}$, N=9	14.07	**1.57**	3.21	39.55	13.73
$LBP^{riu2}_{98,2}$, N=5	9.26	13.21	20.62	21.27	14.14
$LBP^{riu2}_{98,2}$, N=7	9.80	25.50	21.33	**3.45**	8.88
$LBP^{riu2}_{98,2}$, N=9	9.51	1.68	2.61	14.97	**7.89**
DWT, db2, $\beta = 1$, N=5	6.00	7.05	2.59	6.72	24.73
DWT, db2, $\beta = 1$, N=7	6.67	6.98	14.22	5.06	19.14
DWT, db2, $\beta = 1$, N=9	8.09	6.81	11.87	4.84	16.41
DWT, db2, $\beta = 2$, N={5,7}	7.21	4.93	3.86	6.24	16.18
DWT, haar, $\beta = 1$, N=5	5.85	8.10	3.41	11.26	22.87
DWT, haar, $\beta = 1$, N=7	6.41	8.70	4.80	8.98	19.30
DWT, haar, $\beta = 1$, N=9	8.45	8.35	12.77	7.08	17.12
DWT, haar, $\beta = 2$, N={5,7}	7.92	6.93	12.64	8.40	16.28
HUF, db2, $\beta = 1$, N=5	8.10	23.50	21.76	8.16	15.82
HUF, db2, $\beta = 1$, N=7	4.84	7.61	24.29	8.77	20.80
HUF, db2, $\beta = 1$, N=9	8.48	5.91	**2.38**	9.52	20.37
HUF, db2, $\beta = 2$, N={5,7}	6.52	7.64	6.88	8.60	15.67
HUF, haar, $\beta = 1$, N=5	8.19	10.00	26.23	13.72	25.52
HUF, haar, $\beta = 1$, N=7	**3.90**	10.02	23.96	8.48	24.82
HUF, haar, $\beta = 1$, N=9	9.04	5.84	8.94	12.07	22.59
HUF, haar, $\beta = 2$, N={5,7}	6.90	7.01	10.70	9.03	15.61
GLCM, $q = 8$, $d = 1$, N=5	10.27	10.69	20.13	47.10	18.51
GLCM, $q = 8$, $d = 1$, N=7	9.11	9.18	22.06	29.99	19.51
GLCM, $q = 8$, $d = 1$, N=9	9.75	7.05	16.85	21.94	17.01
GLCM, $q = 8$, $d = 2$, N=5	11.79	14.35	35.53	65.26	24.61
GLCM, $q = 8$, $d = 2$, N=7	36.31	17.81	22.04	25.63	36.27
GLCM, $q = 8$, $d = 2$, N=9	39.44	15.93	26.68	39.58	26.08

Table 7: Evaluation of solid texture segmentations using the normalized partition distance (texture with 3 classes). For each texture, the bold values show the best evaluation values (the best segmentation).

Methods	(k)	(l)	(m)	(n)	(o)
$LBP^{riu2}_{26,1}$, N=5	38.05	12.19	58.12	57.72	43.08
$LBP^{riu2}_{26,1}$, N=7	40.27	15.27	53.08	47.10	27.92
$LBP^{riu2}_{26,1}$, N=9	33.06	1.57	52.25	51.42	30.32
$LBP^{riu2}_{98,2}$, N=5	39.01	13.21	43.36	51.09	44.26
$LBP^{riu2}_{98,2}$, N=7	32.09	4.76	32.47	46.52	40.07
$LBP^{riu2}_{98,2}$, N=9	22.41	16.41	42.02	48.51	28.18
DWT, db2, $\beta = 1$, N=5	25.36	9.82	30.10	34.54	28.72
DWT, db2, $\beta = 1$, N=7	19.99	10.10	29.19	27.66	29.22
DWT, db2, $\beta = 1$, N=9	**17.45**	11.99	26.40	**25.55**	29.06
DWT, db2, $\beta = 2$, N={5,7}	18.27	13.93	29.73	25.58	21.90
DWT, haar, $\beta = 1$, N=5	32.08	13.11	38.67	31.78	28.63
DWT, haar, $\beta = 1$, N=7	22.90	10.78	34.36	29.09	22.61
DWT, haar, $\beta = 1$, N=9	21.08	12.22	31.15	27.70	25.03
DWT, haar, $\beta = 2$, N={5,7}	22.00	13.09	31.48	31.41	20.00
HUF, db2, $\beta = 1$, N=5	31.16	8.60	41.66	51.81	31.23
HUF, db2, $\beta = 1$, N=7	30.77	9.88	26.35	40.22	20.47
HUF, db2, $\beta = 1$, N=9	19.12	**1.14**	24.81	32.22	**10.19**
HUF, db2, $\beta = 2$, N={5,7}	22.03	2.41	13.43	40.17	20.10
HUF, haar, $\beta = 1$, N=5	40.23	10.56	34.50	59.80	34.35
HUF, haar, $\beta = 1$, N=7	33.30	8.54	28.79	50.30	16.16
HUF, haar, $\beta = 1$, N=9	30.54	4.43	**10.92**	29.90	26.34
HUF, haar, $\beta = 2$, N={5,7}	20.02	3.36	15.44	40.34	17.75
GLCM, $q = 8$, $d = 1$, N=5	34.63	13.39	39.92	54.53	41.50
GLCM, $q = 8$, $d = 1$, N=7	38.80	12.59	46.18	49.98	34.46
GLCM, $q = 8$, $d = 1$, N=9	36.76	14.76	40.39	45.80	33.88
GLCM, $q = 8$, $d = 2$, N=5	43.30	19.25	32.25	61.31	46.40
GLCM, $q = 8$, $d = 2$, N=7	40.38	17.04	49.05	55.69	48.89
GLCM, $q = 8$, $d = 2$, N=9	41.77	15.75	43.00	57.89	46.27

Table 8: Evaluation of solid texture segmentations using the normalized partition distance (texture with 4 classes). For each texture, the bold values show the best evaluation values (the best segmentation).

Methods		(a)	(b)	(c)	(d)	(e)
LBP	mean	**2.21**	**0.59**	**2.31**	1.78	24.17
	std	2.24	0.13	0.96	1.04	5.60
DWT	mean	2.60	0.92	2.53	**1.52**	20.38
	std	0.44	0.70	0.79	1.04	7.52
HUF	mean	2.34	1.40	7.18	1.78	**20.34**
	std	1.85	0.77	5.00	0.67	6.95
GLCM	mean	4.46	24.16	14.64	12.79	32.68
	std	6.96	22.28	7.14	15.53	2.32
		(f)	(g)	(h)	(i)	(j)
LBP	mean	10.35	8.94	9.58	20.67	**12.18**
	std	1.83	9.15	8.94	12.63	3.54
DWT	mean	7.07	**7.23**	**8.27**	**7.32**	19.00
	std	0.99	1.18	5.00	2.14	3.24
HUF	mean	**6.99**	10.77	15.61	9.78	20.15
	std	1.83	6.42	9.35	2.00	4.07
GLCM	mean	19.44	12.50	23.88	38.25	23.66
	std	14.33	4.18	6.53	16.14	7.12
		(k)	(l)	(m)	(n)	(o)
LBP	mean	34.14	10.56	46.88	50.33	35.63
	std	6.62	6.00	9.35	4.11	7.65
DWT	mean	**22.39**	11.88	31.38	**29.16**	25.64
	std	4.65	1.50	3.70	3.18	3.74
HUF	mean	28.39	**6.11**	**24.48**	43.09	**22.07**
	std	7.35	3.68	10.72	10.16	8.05
GLCM	mean	39.27	15.46	41.79	54.20	41.90
	std	3.21	2.44	5.82	5.56	6.45

Table 9: Mean and standard deviation of the normalized partition distance obtained with segmentation results in Tables 6, 7 and 8 where different parameters of the LBP, DWT, HUF and GLCM methods are tested.

the results of the 3D GLCM and 3D LBP methods. Different neighborhoods ($N = \{5, 7, 9\}$) were tested and no single neighbourhood was best for all types of textures. The data in the tables 6, 7 and 8, indicate that the neighbourhood parameter is the parameter that produces the most significant performance variation independently of the texture method used. To obtain good segmentation performance, this parameter must be adapted to include the patterns inside a texture. It is necessary to use a large neighbourhood to segment macro-textures and a smaller neighbourhood to segment micro-textures. When the neighbourhood is adapted to the image content, we can observe, for the HUF method, low variations of segmentation results according to the type of wavelet used (i.e. Haar or Daubechies). Another parameter of our method is the number of decomposition levels. In table 6, 7 and 8, some segmentations were realized using 2 levels of decomposition. The results obtained using 2 levels were not always the best, but they were often of good quality. If for one level of decomposition a good segmentation was obtained, then the contribution of a second level of decomposition was not always significant. However, for some complex textures, the second level of decomposition did improve the results.

In this section, the performance of the proposed system has been demonstrated through segmentation experiments. The results obtained using the HUF method are similar to the DWT and superior to those obtained using the LBP method, which are known to be very efficient. **The advantages of using the HUF method, in comparison to DWT or LBP, come from the proposed perceptual features that enable an interaction between the segmentation system and an operator. This possibility is crucial in our opinion. To provide a more generic framework, it seems essential to develop understandable feature to facilitate feature selection and contents interpretation.** In the following section, the proposed multiresolution framework is tested on a real-world problem.

6 Usability of the HUF framework in a real-world application

As describe in the introduction, our objective is to provide an interactive system that enables the user to combine human understandable features for the segmentation and characterisation of volumetric textures. In this section, we first describe the architecture of an interactive seg-

mentation system based on HUF features. Then, to demonstrate the usefulness and adaptability of this framework, different application scenarios are presented to extract the regions of interest in 3D ultrasound images of the skin.
The objective of this section is not to validate the superiority of HUF, but rather to demonstrate the usefulness of understandable features when letting the user choose the ones he considers the most appropriate for a specific problem. The different segmentation scenarios presented in this section have been defined in collaboration with three specialists in sonography that have accepted to evaluate the proposed framework.

6.1 Architecture of the segmentation system

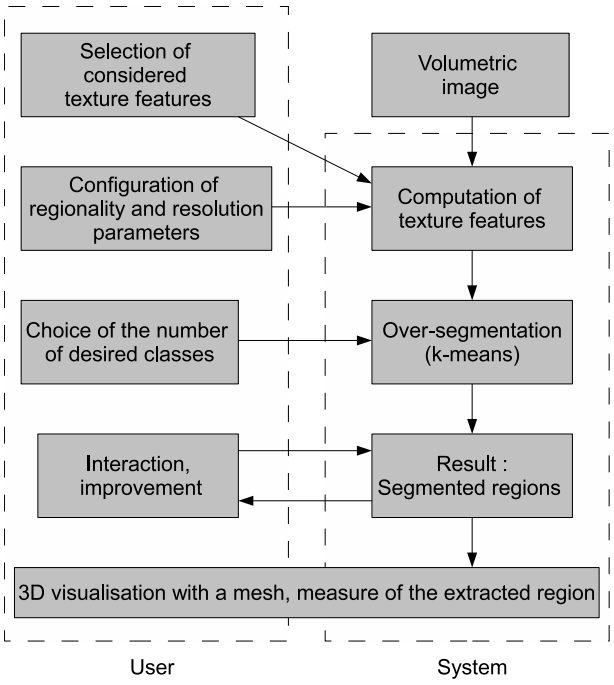

Fig. 9: The different interactive steps of a segmentation process using our software.

The architecture of the system is composed of three primary modules (Figure 9). The first module allows one to compute the HUF features depending on user defined parameters. HUF features are then used by the second segmentation module and the resulting segmented image can be exploited by a 3D visualisation and manipulation module. The segmentation results can then be visualised and improved in an interactive way. It is also possible to represent segmented regions using a mesh and to compute volume information to help specialists in their diagnostic.
Before the segmentation, the user must select the features relevant to be processing of a 3D image. It is also necessary to define supplementary parameters such as the regionality (the neighborhood of a voxel) and the number of resolutions to consider during the HUF feature extraction. A graphic interface allows the user to define these choices. The selected features, the parameters and the processed volumetric image are then used during the feature computation. For each voxel, the selected textural features are computed for the specified region size and the number of resolutions. The segmentation module receives the set of computed feature vectors for each voxel and, then, a first segmentation is generated using the k-means algorithm [74]. By default, a large number of classes is generated (k=15 to obtain an over-segmentation), but this number can be modified by the user. An interactive step allows the user to refine the initial segmentation results. Two region merging operations are available: one uses a hierarchical ascendant classification applied to the centroid of each initial class, and the other operation uses a graph representation of the segmented image. As we have seen subsection 5.2.1, the hierarchical ascendant classification uses the texture feature centroid values of each class. In each step, the two most similar classes are merged. In this manner, the user can improve the current segmentation by increasing or decreasing the number of classes. By exploiting a region adjacency graph representation of the segmentation, the user can also improve the initial segmentation (Figure 12 and Figure 13). The vertices of the graph are positioned using the centre of gravity of each region in the segmented image. Two vertices are connected if the two corresponding regions are adjacent. The merging operation using the graph is manual and allows the user to merge two regions by clicking on the corresponding edge. The motivation for using a graph in the segmentation process is that it provides the ability to focus on a particular region of a 3D image. Moreover, each vertex contains information (such as the average of the features of a region and, the volume of a region) that aids the sonography specialist in perfecting a diagnostic. Using this graph, it is then possible to merge the selected regions, but it is also possible to split regions into subparts. The user can choose a vertex and re-run, a segmentation (a k-means clustering) only on the voxels of the corresponding region.

6.2 Ultrasound images of the skin

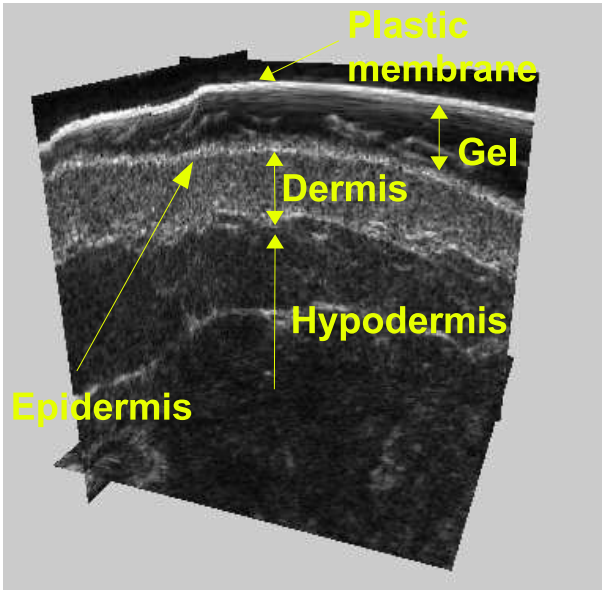

Fig. 10: Example of a three-dimensional image of the skin obtained with 20 MHz ultrasound scanner (Atys Medical France).

Currently, manufacturers produce echographic systems with resolution ranging from 30 to 100 μm. These resolutions require ultrasonic frequencies that range from 20 to 60 MHz. The resolution provided by high frequency ultrasounds enables one to perfectly observe the skin, especially the dermis which has an average thickness between 1 and 2 mm. While it is also possible to similarly explore part of the hypodermis, the available resolutions are insufficient to properly observe the epidermis (Figure 10). The thickness of the epidermis varies between 0.05 and 0.3 mm, thus, ultrasound frequencies greater than 80 MHz are required. Sonography of the skin enables the visualisation of tumours (cysts, nevi, melanomas, and basal cell carcinomas (BCC), for example), inflammatory pathologies and scars. Discriminating among the different types of lesions is not always easy, and cutaneous sonography is undeniably helpful for detection and diagnosis. The possibility of segmenting and characterising a lesion in 3D is very useful for establishing therapeutic strategies. 3D sonography of the skin is rarely used because of the lack of three-dimensional image analysis tools, but the recent evolution of 3D probes should enable the development of new techniques. Using 3D acquisition, it is possible to obtain features that are inaccessible in 2D. Moreover, 3D sonography is well adapted for supervising the evolution of a structure or a lesion, notably by using volume measures.

Ultrasound techniques have several advantages compared with other types of methods, such as magnetic resonance imaging (MRI), X-ray computed tomography (CT). Ultrasounds do not involve any form of ionisation (and are thus harmless to the patients), and the results can be displayed in real time using relatively inexpensive equipment. Nevertheless, current diagnostics are operator-dependent, and the complexity of image interpretation, necessitates the involvement of sonography specialists.

The segmentation of ultrasound images depends on the quality of the acquisition process [77]. The images contain artefacts and variations (speckles, signal attenuation, absence of boundaries, for example) related to the ultrasound propagation phenomena that complicate the segmentation process. The distribution of scatterers and their volumes relative to the wavelength of the incident ultrasound pulse produces various 3D texture patterns. Echogenicity is the ability of a cellular tissue to create an echo. In an echographic image, echogenic zones contain a large number of white 3D patterns, which are an important characteristic used by specialists to identify pathologies. This characteristic is the reason why sonography specialists use the echogenicity (which corresponds to texture information) to describe the structures inside ultrasound images.

6.3 Interest of a user-guided segmentation

To segment an image, different scenarios can be conceived. Here we present two examples for a 3D ultrasound image of skin with a nevus. In the first scenario (Figure 12), the first step of the segmentation process is a splitting operation of the image into two different classes (Figure 12(a)). The image is then divided into two classes in which several regions can be identified. Inside this first segmentation, different areas of the skin, including a part of the nevus, are identified. To obtain a complete representation of the nevus, a new splitting operation is run on the region around the nevus. A second area appears in the central part of the segmentation (Figure 12(b)). Next, a splitting operation is performed by the user, which allows the extraction of the external part of the nevus (Figure 12(c)). To yield an exact representation of the nevus, a merging operation is required to regroup the two identified regions (Figure 12(d)).

In the second scenario, the user starts the segmentation by performing an over-segmentation using the splitting operation with six classes (Figure 13(a)). As demonstrated by the first segmentation (Figure 13(a)), the

nevus is composed of three different regions. To extract the nevus as one unique region, two successive merging operations are performed by the user (Figure 13(b) and Figure 13(c)). It is then possible to extract the nevus inside the ultrasound image (Figure 11(b) and Figure 11(c)). The two resulting meshes are very similar. This similarity was found in most of our experiments and demonstrates the robustness of the proposed segmentation system.Using the Dice coefficient [78], Table 10 compares the segmentation of the images in Figure 11(a), 14 and 19 obtained using two different scenarios.

Images	11(a)	14	19
Dice coefficient	0.934	0.948	0.979

Table 10: Comparison of different segmentation scenarios with the Dice coefficient.

The Dice coefficient is a similarity measure that is defined for two sets X and Y as follows:

$$\textbf{Dice coefficient} = \frac{2\,|X \cap Y|}{|X| + |Y|} \tag{15}$$

Its value is 1 if the two sets are similar. The results presented in Table 10 show that segmentations obtained with different scenarios are very similar and demonstrate the robustness of our system.

6.4 Interest of a user feature selection

This system has been proposed to three specialists in sonography in order to segment various pathologies, organs, etc. The segmentation results obtained for three different 3D ultrasound images are presented Figure [15,17,18,20,22,23,24]: Image Figure 14 contains a nevus, Image Figure 19 a histiocytofibroma, and Image Figure 24(a) a tendon. As for images Figure 14 and Figure 19, segmentations have been generated using the features introduced in the previous section: the HUF method, the 3D LBP algorithm and the 3D Haralick features. For the Nevus and Histiocytofibroma images, the best segmentation results and the extracted pathologies are presented using a mesh representation. The following parameters were used: the $LBP^{riu2}_{26,1}$ operator was used for the 3D LBP algorithm, the 3D GLCM method used the parameters $d = 1$ and $q = 8$ and the HUF method used the Daubechies wavelet (db2) for one level of decomposition. For all these texture analysis methods, the proposed graph representation was used to enable interactive improvement of the segmentation. The set of methods used a region size $N = 7$ which allows one to obtain accurate results for this type of image. The results demonstrate the capacity of our software to isolate different types of pathologies according to the choices made by users.
To obtain the segmentations presented in image Figure 15 and image Figure 20, four systems were presented to three sonography specialists: system 1 used all of the HUF features except the directionality (because the zones of interests have no anisotropic properties), system 2 used only the contrast and volume of the HUF features, system 3 used the GLCM features, and system 4 used the LBP features. To evaluate the segmentations, we asked the specialists to rank the best segmentations (see Table 11) obtained with the different methods: HUF using all of the features except directionality (HUFa), HUF using only the contrast and the volume features (HUFb), LBP and GLCM.

	HUFa	HUFb	LBP	GLCM
Image 14	1	3	4	2
Image 19	1	3	4	2

Table 11: Ranking of different segmentations obtained by using different set of features: HUF using all the feature expect directionality (HUFa), HUF using only the contrast and the volume (HUFb), LBP and GLCM.

For the two segmented images, the 3D LBP method ranked worst because the regions of interest (nevus or histiocytofibroma) were not identified. Intensity variation is essential information in this type of image, and the LBP method is not sensitive to this property; this deficiency caused unsatisfactory results. When all of the discriminant features in the ultrasound images (which were well selected according to a priori knowledge) were used, the HUF method obtained the best ranking, followed by the GLCM method. When features that are discriminating for a given image are omitted, the quality of the obtained segmentation is not as good. This was the case when only the contrast and volume features of the HUF framework were used for segmentation of images Figure 14 and 19.
Figure 24 shows a 3D ultrasound image of a tendon. Different images of the results yielded by the HUF method are shown: Figure 24(b) was generated using all of the HUF features except the directionality, and the results shown in Figures 24(d), 24(e) and 24(f) were obtained using all seven perceptual features, including the directionality. One level of decomposition ($\beta = 1$) was used to obtain the segmentation shown in Figure 24(d), two levels of decomposition ($\beta = 2$) were used for the seg-

(a) 3D ultrasound image with a nevus

(b) Mesh representation of the nevus segmented with the scenario proposed in Figure 12.

(c) Mesh representation of the nevus segmented with the scenario proposed in Figure 13.

Fig. 11: Segmentation results of a 3D ultrasound image of the skin using two different scenarios.

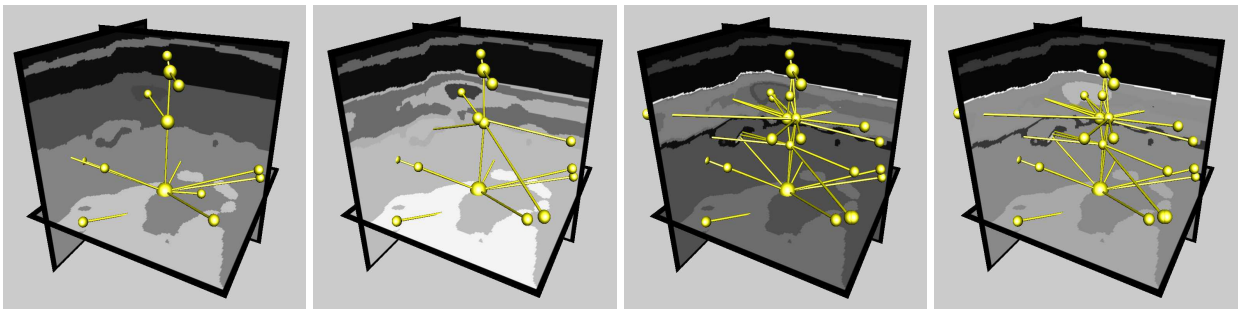

(a) Splitting, 2 classes (b) Splitting, 2 classes (c) Splitting, 2 classes (d) Merging

Fig. 12: Scenario 1: Figure 11(a) is segmented using four operations: three splitting operations and one merging operation. Vertices represent regions that have been identified during the segmentation process and an edge links two vertices if their corresponding regions are adjacent. The users perform merging and splitting operations by clicking on specific vertices or edges in the graph (see sub-section 6.1 for more details).

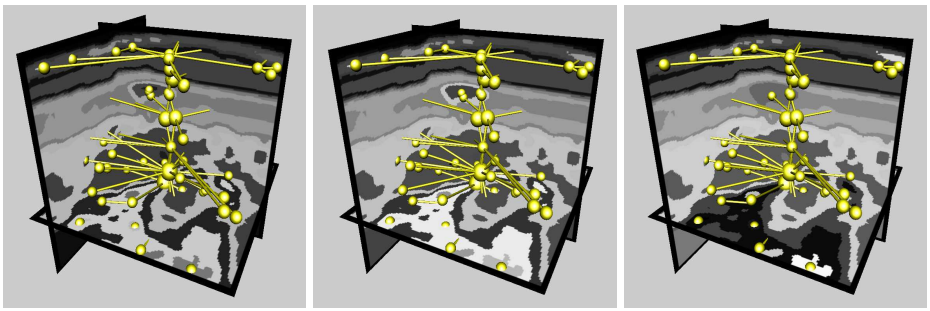

(a) Splitting, 6 classes (b) Merging (c) Merging

Fig. 13: Scenario 2: Figure 11(a) is segmented using three operations: one splitting operation and two merging operation. Vertices represent regions that have been identified during the segmentation process and an edge links two vertices if their corresponding regions are adjacent. The users perform merging and splitting operations by clicking on specific vertices or edges in the graph (see sub-section 6.1 for more details).

mentation shown in Figure 24(e) and three levels of decomposition ($\beta = 3$) were used for the segmentation shown in figure 24(f). Figure 24(c) demonstrates that it was not possible to isolate the tendon without using the directionality feature. Indeed, directionality is the main property that distinguishes a tendon which contains an important anisotropy. Using the information about directionality, and one level of decomposition, the segmentation shown in Figure 24(d) was obtained; this enabled the isolation of the tendon (figure 24(g)). When the number of resolutions was increased, the segmentations obtained were more accurate: with two res-

olutions, the tendon is more uniform (Figure 24(h)) and with three resolutions, the segmentation is cleaner and only the tendon is isolated (Figure 24(i)). For the images presented in Figures 14 and 19, it was unnecessary to use several resolutions because the quality of the obtained segmentation was sufficient when only one resolution was used. The contribution of several resolutions is thus demonstrated to be insignificant.

To conclude, we note the very interesting performance of our HUF method indicated by the qualitative analysis of the results. The classical GLCM method is an efficient method for the processing of ultrasound textures [77]; however, according to the specialists, our system obtained superior results. In this section, the results were qualitatively evaluated by sonography specialists through visual comparisons between different segmentations. The reason is that it is very difficult to produce a 3D ground truth because of construction difficulties in 3D ultrasound images which are too time-costly and generate precision issues. Without a suitably precise ground truth, it is impossible to produce a pertinent quantitative evaluation.
From a functional point of view, the perceptual features are very interesting for feature selection and content interpretation. Moreover, the proposition of a region adjacency graph representation of the segmented image enables significant interaction with the operator. According to the specialists, the splitting and merging operations allow the user to efficiently guide the segmentation process. Consequently, the proposed system is robust regardless of the type of processed image.

7 Conclusion

The primary contribution of this paper is the proposition of a multiresolution system that combines perceptual features for the analysis of 3D textured images, also known as volumetric or solid textures. We have proposed a set of perceptual features that are easily understandable by humans: granularity, contrast, volume, compactness, regularity, directionality and roughness. To define this set of features, we tried to select simple yet complementary features from those commonly used by humans. The computational process from the proposed descriptors combines frequency methods with the discrete wavelet transform and a geometrical method that uses 3D connected component extraction. Connected components are identified using a succession of binary images that are determined using a clustering approach; this method significantly increases the robustness of the proposed geometrical features. By combining several families of texture analysis methods, the HUF framework provides a rich and robust multiresolution description of textures that requires a reasonable computation time. To analyse the pertinence of our perceptual features and their correspondence with human descriptions of volumetric textures, psychological experiments have been presented; the experiments demonstrates a significant correlation between human and feature rankings. Using segmentation experiments, the performance of the proposed system has been compared with the performance of other methods proposed in the literature, including the 3D GLCM, 3D DWT and 3D LBP methods. Whereas the 3D LBP method, the 3D DWT method and the HUF method obtain similar results when processing relatively simple solid textures, the HUF and 3D DWT methods produce segmentations of higher quality as the volumetric textures' complexity increases. The usability of the proposed framework has been illustrated for the medical field. A software system that use our HUF features to segment 3D ultrasound images has been presented to sonography specialists. The proposed system allows the user to interact with and manipulate a graph representation of the 3D image using information provided by the initial segmentation. This graph enables the user to considerably improve the segmentation and offers different possibilities to the users, who can thus merge regions of interest or focus their attention on a given region. Using understandable features is very important because it enables the user to select or unselect pertinent or non pertinent features according to the content of the images. To the best of our knowledge, no other work has presented a comparably sophisticated combination of perceptual texture features for volumetric texture analysis. We hope that this proposition, the data provided and the experimental results will be useful for future work.

Of course, several improvements could be made in future work. To complete our segmentation system, we might exploit *a priori* knowledge (such as atlas and topological information). Using graphs, it could be interesting to compare the obtained segmentation to *a priori* knowledge to revisit the segmentation and to be more conventional to the supposed image content. Improvement of the user interaction using the region adjacency graph is also conceivable.

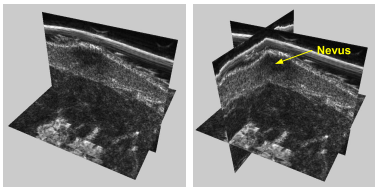

(a) (b)

Fig. 14: 3D ultrasound image of the skin with a nevus. Segmentation of this image are presented Figure 15,16,17 and 18 where different segmentation methods have been used.

(a) (b) (c)

Fig. 15: Best segmentation of the image in Figure 14 obtained with system 1: the HUF method with all the HUF features except the directionality. Each region is represented by a specific gray-level value.

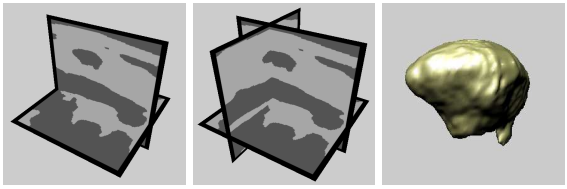

(a) (b) (c)

Fig. 16: Best segmentation of the image in Figure 14 obtained with system 2: the HUF method with only the Contrast and the Volume features. Each region is represented by a specific gray-level value.

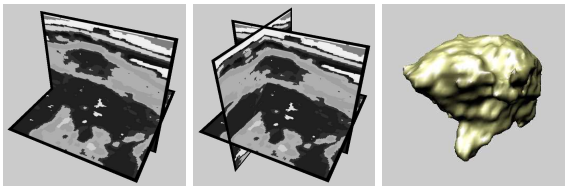

(a) (b) (c)

Fig. 17: Best segmentation of the image in Figure 14 obtained with system 3: 3D GLCM features. Each region is represented by a specific gray-level value.

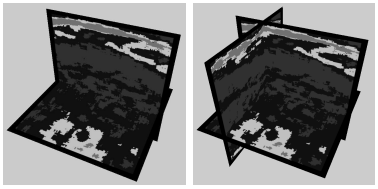

(a) (b)

Fig. 18: Best segmentation of the image in Figure 14 obtained with system 4: 3D LBP features. Each region is represented by a specific gray-level value. The nevus has not been identified (see sub-section 6.4 for more details).

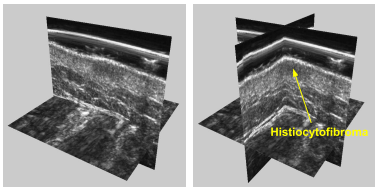

(a) (b)

Fig. 19: 3D ultrasound image with a histiocytofibroma. Segmentation of this image are presented Figure 20,21,22 and 23 where different segmentation methods have been used.

(a) (b) (c)

Fig. 20: Best segmentation of the image in Figure 19 obtained with system 1: the HUF method with all the HUF features except the directionality. Each region is represented by a specific gray-level value.

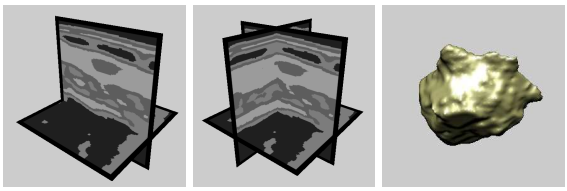

(a) (b) (c)

Fig. 21: Best segmentation of the image in Figure 19 obtained with system 2: the HUF method with only the Contrast and the Volume features. Each region is represented by a specific gray-level value.

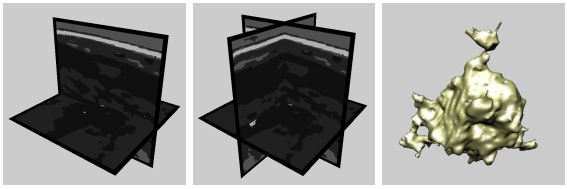

(a) (b) (c)

Fig. 22: Best segmentation of the image in Figure 19 obtained with system 3: 3D GLCM features. Each region is represented by a specific gray-level value.

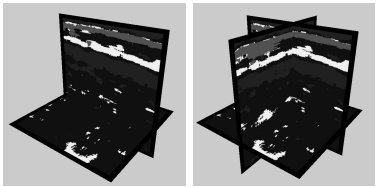

(a) (b)

Fig. 23: Best segmentation of the image in Figure 19 obtained with system 4: 3D LBP features. Each region is represented by a specific gray-level value. The histiocytofibroma has not been identified (see sub-section 6.4 for more details).

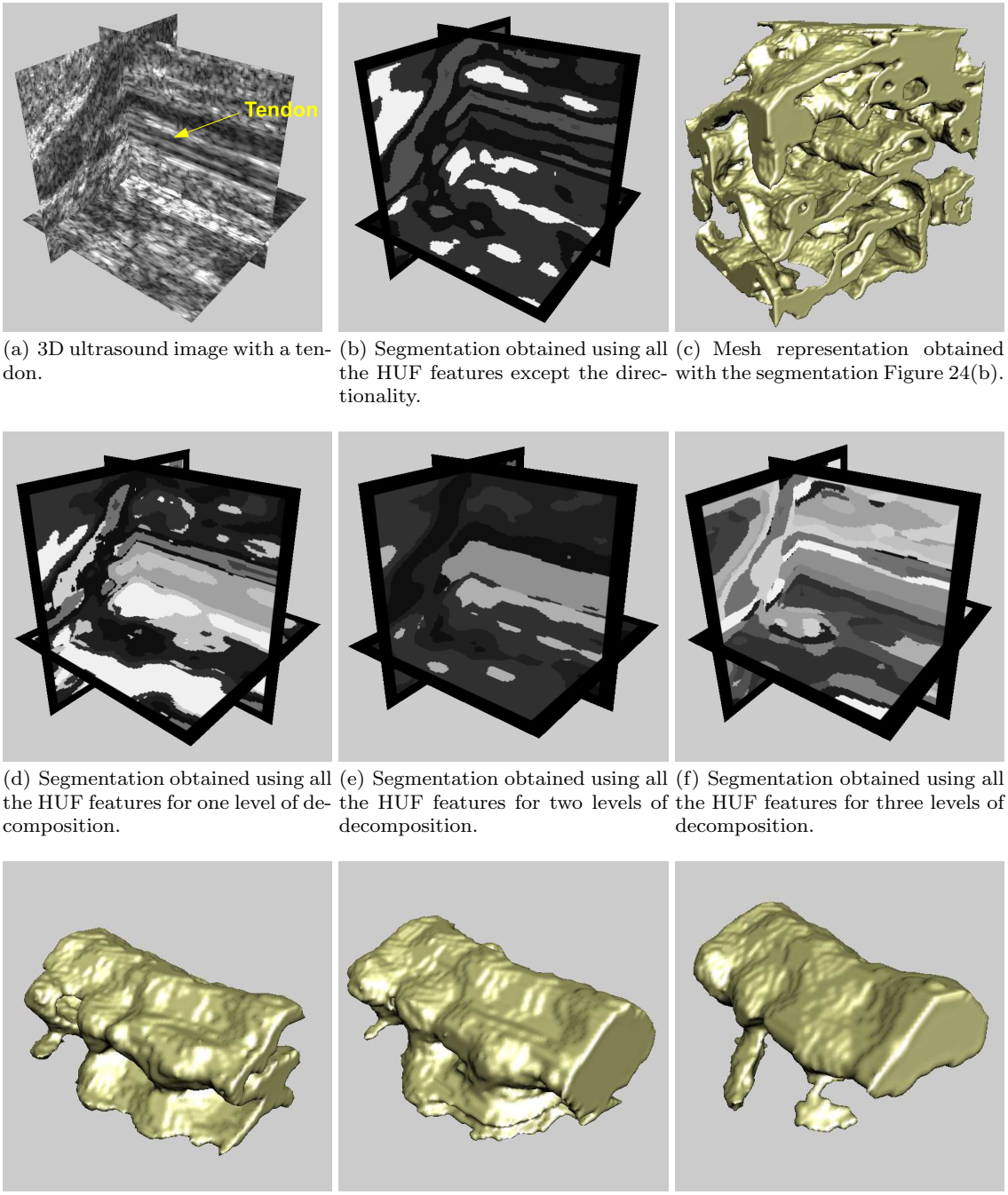

(a) 3D ultrasound image with a tendon.

(b) Segmentation obtained using all the HUF features except the directionality.

(c) Mesh representation obtained with the segmentation Figure 24(b).

(d) Segmentation obtained using all the HUF features for one level of decomposition.

(e) Segmentation obtained using all the HUF features for two levels of decomposition.

(f) Segmentation obtained using all the HUF features for three levels of decomposition.

(g) Mesh representation obtained with the segmentation Figure 24(d).

(h) Mesh representation obtained with the segmentation Figure 24(e).

(i) Mesh representation obtained with the segmentation Figure 24(f).

Fig. 24: Segmentation set of a 3D echographic image with the HUF method (tendon localization).

References

1. Mihran Tuceryan and Anil K. Jain. *Texture Analysis*, chapter 2.1, pages 207–248. The Handbook of Pattern Recognition and Computer Vision, 1998.
2. Robert M. Haralick. Statistical and structural approaches to textures. *Proceedings of the IEEE*, 67(5):786–804, May 1979.
3. Robert M. Haralick, K. Shanmugam, and I. Dinstein. Texture features for image classification. *IEEE Transactions on Systems, Man, and Cybernetics*, 3(6):610–621, 1973.
4. Mihran Tuceryan and Anil K. Jain. Texture segmentation using voronoi polygons. *IEEE Transactions on Pattern Analysis and Machine Intelligence*, 12:211–216, February 1990.
5. Stephane G. Mallat. A theory for multiresolution signal decomposition: the wavelet representation. *IEEE Transactions on Pattern Analysis and Machine Intelligence*, 11:674–693, 1989.
6. Rama Chellappa and Anil K. Jain. *Markov Random Fields Theory and Application*. Academic Press, 1993.
7. Hideyuki Tamura, Shunji Mori, and Takashi Yamawaki. Texture features corresponding to visual perception. *IEEE Transactions on Systems, Man, and Cybernetics*, 8(6):460–473, 1978.
8. Moses Amadasun and Robert King. Texture features corresponding to textural properties. *IEEE Transactions on Systems, Man, and Cybernetics*, 19(5):1264–1274, September/October 1989.
9. Fabrice Neyret. *Homepage of Neyret*, 1996. `http://www.evasion.imag.fr/Membres/Fabrice.Neyret/`.
10. Motofumi T. Suzuki, Yaginuma Yoshitomo, Noritaka Osawa, and Yuji Y. Sugimoto. Classification of solid textures using 3D mask patterns. In *ICSMC '04: Proceedings of the IEEE International Conference on Systems, Man and Cybernetics*, 2004.
11. Constantino Carlos Reyes-Aldasoro and Abhir Bhalerao. Volumetric texture segmentation by discriminant feature selection and multiresolution classification. *IEEE Transactions on Medical Imaging*, 26:1–14, 2007.
12. Linlin Shen and Li Bai. 3D Gabor wavelets for evaluating spm normalization algorithm. *Medical Image Analysis*, 12:375–383, 2008.
13. Nico Pietroni, Paolo Cignoni, Miguel A. Otaduy, and Roberto Scopigno. Solid-texture synthesis: A survey. *IEEE Computer Graphics and Applications*, 30:74–89, 2010.
14. Constantino Carlos Reyes-Aldasoro and Abhir Bhalerao. Volumetric texture analysis in biomedical imaging. In *Biomedical diagnostics and clinical technologies : applying high-performance cluster and grid computing*, 2011.
15. Oana G. Cula and Kristin J. Dana. 3D texture recognition using bidirectional feature histograms. *International Journal of Computer Vision*, 59(1):33–60, 2004.
16. Fabrice Neyret. A general and multiscale model for volumetric textures. In Wayne A. Davis and Przemyslaw Prusinkiewicz, editors, *GI '95: Proceedings of Graphics Interface*, pages 83–91. Canadian Information Processing Society, Canadian Human-Computer Communications Society, May 1995. ISBN 0-9695338-4-5.
17. Gianfranco Doretto, Alessandro Chiuso, Ying Nian Wu, and Stefano Soatto. Dynamic textures. *International Journal of Computer Vision*, 51(2):91–109, 2003.
18. Ludovic Paulhac, Pascal Makris, Jean-Marc Gregoire, and Jean-Yves Ramel. Human understandable features for segmentation of solid texture. In *ISVC '09: Proceedings of the 5th International Symposium on vision computing*, pages 379–390, 2009.
19. Vassili A. Kovalev, Maria Petrou, and Yaroslav S. Bondar. Texture anisotropy in 3D images. *IEEE Transactions on Image Processing*, 8:346–360, 1999.
20. Horace Ho-Shing IP and Stephen Wang-Cheung Lam. Using an octree-based rag in hyper-irregular pyramid segmentation of texture volume. In *IAPR '94: Proceedings of the IAPR Workshop on Machine Vision Applications*, pages 259–262, Kawasaki, Japan, December 1994.
21. Vassili A. Kovalev, Frithjof Kruggel, Hermann-Josef Gertz, and D. Yves von Cramon. Three-dimensional texture analysis of MRI brain datasets. *IEEE Transactions on Medical Imaging*, 20(5):424–433, 2001.
22. Vassili A. Kovalev, Maria Petrou, and John Suckling. Detection of structural differences between the brains of schizophrenic patients and controls. *Psychiatry Research: NeuroImaging*, 124(3):177–189, 2003.
23. Doaa Mahmoud-Ghoneim, Grégoire Toussaint, Jean Marc Constans, and Jacques D. de Certaines. Three dimensional texture analysis in MRI: a preliminary evaluation in gliomas. *Magnetic Resonance Imaging*, 21:983–987, 2003.
24. Xiang Chen and Robert F. Murphy. Robust classification of subcellular location patterns in high resolution 3D fluorescence microscope images. In *EMBS'04 : Proceedings of the International Conference on Engineering in Medicine and Biology Society*, number 1-5, September 2004.
25. Chad Showalter, Bradley D. Clymer, Bradford Richmond, and Kimerly Powell. Three-dimensional texture analysis of cancellous bone cores evaluated at clinical ct resolutions. *Osteoporos International*, 17:259–266, 2006.
26. Kourosh Jafari-Khouzani, Hamid Soltanian-Zadeh, Kost Elisevich, and Suresh Patel. Comparison of 2D and 3D wavelet features for TLE lateralization. In *Proceedings of the SPIE*, volume 5369, 2004.
27. Yiqiang Zhan and Dinggang Shen. Deformable segmentation of 3D ultrasound prostate image using statistical texture matching method. *IEEE Transactions on Medical Imaging*, 25(3):256–272, march 2006.
28. Margarita Fernández, Adriana Mavilio, and Manuel Tejera. Texture segmentation of a 3D seismic section with wavelet transform and Gabor filters. In *ICPR '00: Proceedings of the international Conference on Pattern Recognition*, volume 3, pages 354–357, Barcelona, Spain, 2000.
29. Rousseau François, Ronan Fablet, and Christian Barillot. Robust statistical registration of 3D ultrasound images using texture information. In *ICIP '03: Proceedings of the international Conference on Image Processing*, volume 1, September 2003.
30. Gérard G. Medioni and Yoshio Yasumoto. A note on using the fractal dimension for segmentation. In *WCVRC '84: Proceedings of the workshop on Computer Vision: Representation and Control, Annapolis*, pages 25–30, 1984.
31. Du-Ming Tsai and Chi-Fong Tseng. Surface roughness classification for castings. *Pattern Recognition*, 32:389–405, 1999.
32. F. Luk and Van Minh Huynh. A vision system for in-process surface quality assessment. In *Proceedings of the Vision'87 SME conference*, 1987.
33. G.A. Al-Kindi, R.M. Baul, and K.F. Gill. An application of machine vision in the automated inspection of

engineering surfaces. *International journal of production research*, 30:241–253, 1992.

34. Hu Zhongxiang, Zhu Lei, Teng Jiaxu, Ma Xuehong, and Shi Xiaojun. Evaluation of three-dimensional surface roughness parameters based on digital image processing. *The International Journal of Advanced Manufacturing Technology*, 2008.
35. Dmitry Chetverikov. Pattern orientation and texture symmetry. In *ICCAIP'95: Proceedings of the 6th International Conference on Computer Analysis of Images and Patterns*, 1995.
36. Johann Radon. Uber die bestimmung von funktionen durch ihre integralwerte langs gewisser mannigfaltigkeiten. *Berichte Sachsische Academie der Wissenchaften, Leipzig*, 69:262–267, 1917.
37. Jean-Pierre Guedon, Dominique Barba, and Nicole Burger. Psychovisual image coding via an exact discrete radon transform. In *SPIE '95: proceedings of the international conference of the Society of Photo-Optical Instrumentation Engineers*, volume 2501, pages 562–572, April 1995.
38. Michel Coster and Jean-Louis Chermand. *Precis d'Analyse d'Images*. CNRS, 1989.
39. Richard O. Duda and Peter E. Hart. Use of the hough transformation to detect lines and curves in pictures. *Communications of the ACM*, 15(1):11–15, 1972.
40. Turgut Aydin, Yucel Yemez, Emin Anarim, and Bulent Sankur. Multidirectional and multiscale edge detection via m-band wavelet transform. *IEEE Transactions on Image Processing*, 5(9):1370–1376, 1996.
41. Mickael Unser. Sum and difference histograms for texture classification. *IEEE Transactions on Pattern Analysis and Machine Intelligence*, 8:119–125, 1986.
42. Zhenhua Guo, LeiZhang, and DavidZhang. Rotation invariant texture classification using lbp variance (lbpv) withglobalmatching. *Pattern Recognition*, 2009.
43. André Gagalowicz. *Vers un modèle de texture*. PhD thesis, Université Pierre et Marie Curie, Paris VI, 1983.
44. Soe Win Myint and Nina Lam. A study of lacunarity-based texture analysis approaches to improve urban image classification. *Computers, environment and urban systems*, 29(5):501–523, 2005.
45. Maxim Shoshany. An evolutionary patch pattern approach for texture discrimination. *Pattern Recognition*, 41:2327–2336, 2008.
46. Dinesh P. Mital, Wee Leng Goh, Kap Luk Chan, and R.K. Goyal. A translation rotation and scale invariant texture analysis technique based on image granularity. In *ISRM '94: Proceedings of the Fifth International Symposium on Robotics and Manufacturing*, 1994.
47. R.K. Goyal, Wee Leng Goh, Dinesh P. Mital, and Kap Luk Chan. Invariant element compactness for texture classification. In *ICARCV '94: Proceedings of the International Conference on Automation, Robotics and Computer Vision*, 1994.
48. R.K. Goyal, Wee Leng Goh, Dinesh P. Mital, and Kap Luk Chan. A translation rotation and scale invariant texture analysis technique based on structural properties. In *ICAT '94: Proceedings of the Third International Conference on Automation Technology*, 1994.
49. R.K. Goyal, Wee Leng Goh, Dinesh P. Mital, and Kap Luk Chan. Scale and rotation invariant texture analysis based on structural property. In *IECON '95: Proceedings of the International Conference on Industrial Electronics, Control, and Instrumentation*, 1995.
50. Hsin-Chih Lin, Ling-Ling Wang, and Shi-Nine Yang. Extracting periodicity of a regular texture based on autocorrelation functions. *Pattern Recognition Letters*, 18:433–443, 1997.
51. K. Selkäinaho, Jussi Parkkinen, and Erkki Oja. Comparison of χ^2 and κ statistics in finding signal and picture periodicity. In *ICPR '88: Proceedings of the 9th International Conference on Pattern Recognition*, pages 1221–1224, Rome, Italy, October 1988.
52. Valery V. Starovoitov, Sang-Yong Jeong, and Rae-Hong Park. Texture periodicity detection: Features, properties, and comparisons. *IEEE Transactions on Systems, Man, and Cybernetics*, 28(6):839–849, November 1998.
53. Thomas Leung and Jittendra Malik. Representing and recognizing the visual appearance of materials using three-dimensional textons. *International Journal of Computer Vision*, 43(1):29–44, February 2001.
54. Stéphane Mallat. *A Wavelet Tour of Signal Processing, Third Edition: The Sparse Way*. Academic Press, 2008.
55. Jean-Marc Chassery and Annick Montanvert. *Géométrie discrète en analyse d'images*. 1991.
56. Kesheng Wu, Ekow Otoo, and Kenji Suzuki. Optimizing two-pass connected-component labeling algorithms. *Pattern Analysis and Applications*, 12:117–135, 2009.
57. Jianguo Zhang and Tieniu Tan. Brief review of invariant texture analysis methods. *Pattern Recognition*, 35:735–747, 2002.
58. Johannes Kopf, Chi-Wing Fu, Daniel Cohen-Or, Oliver Deussen, Dani Lischinski, and Tien-Tsin Wong. Solid texture synthesis from 2d exemplars. In *SIGGRAPH '07: Proceedings of the 34th International Conference on Computer Graphics and Interactive Techniques*, 2007.
59. Ludovic Paulhac, Pascal Makris, and Jean-Yves Ramel. A solid texture database for segmentation and classification experiments. In *VISSAPP '09: Proceedings of the Fourth International Conference on Computer Vision Theory and Applications*, 2009.
60. Ludovic Paulhac, Pascal Makris, and Jean-Yves Ramel. Comparison between 2D and 3D local binary pattern methods for characterisation of three-dimensional textures. In *ICIAR '08: Proceedings of the 5th International Conference in Image Analysis and Recognition*, 2008.
61. Phil Brodatz. *Textures: A Photographic Album for Artists and Designer*. Dover Pub., 1966.
62. Trygve Randen and John Hakon Husőy. Filtering for texture classification : A comparative study. *IEEE Transactions on Pattern Analysis and Machine Intelligence*, 21:291–310, 1999.
63. Guy Smith and Ian Burns. *Meastex database*, 1997. `http://www.texturesynthesis.com/meastex/meastex.html`.
64. Jerry Wu. *PMTex database*, 2002. `http://www.taurusstudio.net/research/pmtexdb/compare.htm`.
65. Kristin J. Dana, Bram Van-Ginneken, Shree K. Nayar, and Jan J. Koenderink. *CURet database*, 1999. `http://www.cs.columbia.edu/CAVE/software/curet/index.php`.
66. Timo Ojala, Topi Mäenpää, Matti Pietikäinen, Jaakko Viertola, Juha Kyllönen, and Sami Huovinen. *OUTex database*, 2002. `http://www.outex.oulu.fi/index.php?page=outex_home`.
67. Johannes Kopf. *Solid textures samples*, 2007. `http://johanneskopf.de/publications/solid/textures/index.html`.
68. Luc J. Van Gool, P. Dewaele, and André Oosterlinck. Texture analysis anno 1983. *Computer Vision, Graphics, and Image Processing*, 29(3):336–357, 1985.

69. Ludovic Paulhac. *A solid texture database*, 2009. `http://www.rfai.li.univ-tours.fr/fr/ressources/3Dsynthetic_images_database.html`.
70. Timo Ojala and Matti Pietikäinen. Multiresolution gray-scale and rotation invariant texture classification with local binary patterns. *IEEE Transactions on Pattern Analysis and Machine Intelligence*, 24:971–987, 2002.
71. Ingrid Daubechies. *Ten Lectures on Wavelets*. CBMS-NSF Lecture Notes nr. 61, 1992.
72. Michael Unser. Texture classification and segmentation using wavelet frames. *IEEE Transactions on Image Processing*, 4:1549–1560, 1995.
73. K. Muneeswaran, L. Ganesan, S. Arumugam, and K. Ruba Soundar. Texture classification with combined rotation and scale invariant wavelet features. *Pattern Recognition*, 38:1495–1506, 2005.
74. G.B. Coleman and H.C. Andrews. Image segmentation by clustering. In *Proceedings of the IEEE*, pages 773–785, 1979.
75. Jaime S. Cardoso and Luis Corte-Real. Toward a generic evaluation of image segmentation. *IEEE Transactions on Image Processing*, 14(11):1773–1782, 2005.
76. Dan Gusfield. Partition-distance: A problem and class of perfect graphs arising in clustering. *Information Processing Letters*, 82(9):159–164, 2002.
77. J. Alison Noble and Djamal Boukerroui. Ultrasound image segmentation: A survey. *IEEE Transactions on Medical Imaging*, 25(8):987–1010, August 2006.
78. Lee R. Dice. Measures of the amount of ecologic association between species. *Ecology*, 26:297–302, 1945.